LIMNOLOGY
and
OCEANOGRAPHY: METHODS

Limnol. Oceanogr.: Methods 12, 2014, 651–669

Improving the optimization solution for a semi-analytical shallow water inversion model in the presence of spectrally correlated noise

Rodrigo A. Garcia[1], Lachlan I.W. McKinna[1,2], John D. Hedley[3], and Peter R.C.S. Fearns[1]*

[1]Remote Sensing and Satellite Research Group, Department of Imaging and Applied Physics, Curtin University, GPO Box U1987, Perth, Western Australia, 6845.

[2]NASA Postdoctoral Program Fellow, Ocean Ecology Laboratory, Goddard Space Flight Center, Greenbelt, MD 20771, USA

[3]Environmental Computer Science Ltd. Raymond Penny House, Hammett Square, Tiverton, Devon, EX16 6LR, UK

Abstract

In coastal regions, shallow water semi-analytical inversion algorithms may be used to derive geophysical parameters such as inherent optical properties (IOPs), water column depth, and bottom albedo coefficients by inverting sensor-derived sub-surface remote sensing reflectance, r_{rs}. The uncertainties of these derived geophysical parameters due to instrumental and environmental noise can be estimated numerically via the addition of spectral noise to the sensor-derived r_{rs} before inversion. Repeating this process multiple times allows the calculation of the standard error and average for each derived parameter. Apart from spectral non-uniqueness, the optimization algorithm employed in the inversion must converge onto a single minimum to obtain a true representation of the uncertainty for a given set of noise-perturbed r_{rs}. Failure to do so inflates the uncertainty and affects the average retrieved value (accuracy). We show that the standard approach of seeding the optimization with an arbitrary, fixed initial guess, can lead to the convergence to multiple minima, each having substantially different centroids in multi-parameter solution space. We present the Update-Repeat Levenberg-Marquardt (UR-LM) and Latin Hypercube Sampling (LHS) routines that dynamically search the solution space for an optimal initial guess, that when applied to the optimization allows convergence to the best local minimum. We apply the UR-LM and LHS methods on HICO-derived and simulated r_{rs} and demonstrate the improved computational efficiency, precision, and accuracy afforded from these methods compared with the standard approach. Conceptually, these methods are applicable to remote sensing based, shallow water or oceanic semi-analytical inversion algorithms requiring nonlinear least squares optimization.

The implicit inverse modeling approach is commonly used in optical remote sensing applications to derive geophysical parameters from sensor-observed radiometric data. A typical semi-analytical inversion algorithm comprises of three key components: (i) a forward semi-analytical model, (ii) a set of internal geophysical parameters, and (iii) an inverse spectral optimization method (Werdell et al. 2013). In shallow waters, a forward semi-analytical model simulates the sub-surface remote sensing reflectance, r_{rs}, as a function of the water column's inherent optical properties (IOPs), depth and the bottom albedo coefficients (Maritorena et al. 1994; Lee et al. 1998; Albert and Mobley 2003; Klonowski et al. 2007; Brando et al. 2009). Using an optimization method, the internal geophysical parameters (i.e., IOPs, depth, and bottom albedos) are iteratively varied until the modeled sub-surface remote sensing reflectance, r_{rs}^{M}, best matches the sensor-derived r_{rs}. At this point the set of internal geophysical parameters are deemed the optimal solution.

Two spectral optimization methods implemented by semi-analytical ocean color inversion models are the Levenberg-Marquardt (LM, Marquardt 1963, e.g., Klonowski et al. 2007; Werdell et al. 2013) and Downhill simplex algorithms (Nelder and Mead 1965, e.g., Brando et al. 2009). These optimization algorithms iteratively change the model parame-

*Corresponding author: E-mail: rodrigo.garcia@postgrad.curtin.edu.au

Acknowledgments

This research was supported by an Australian Postgraduate Award administered by Curtin University. The authors would like to thank Dr. Craig Markwardt for his valued advice regarding the MPFIT implementation of the Levenberg-Marquardt optimization routine. The authors also thank the HICO project team at both OSU and NRL for targeting, processing, and distribution of HICO L1B data over Shark Bay. All HICO™ data were provided by the Naval Research Laboratory through the Oregon State University, College of Earth, Ocean, and Atmospheric Sciences' HICO website (hico.coas.oregonstate.edu).

DOI 10.4319/lom.2014.12.651

ters in the direction of the lowest cost function; where the cost function is a measure of the similarity between the forward modeled r_{rs}^{M} and the sensor-derived r_{rs} (see Table!1 for the list of acronyms and symbols used in this text). Thus the objective of these optimization schemes is to find the global minimum, that is, the set of model parameters whose modeled r_{rs}^{M} matches perfectly with r_{rs}. Unfortunately, such optimization algorithms are understood to potentially converge to local minima—rather than the global minimum—particularly if the initial guess used to seed the optimization is sufficiently close to a local minimum (Press et al. 2007; Kirkpatrick et al. 1983).

Several global optimization algorithms have been implemented in the inversion of ocean color data. Maritorena et al. (2002) used a downhill simplex-coupled simulated annealing procedure (see Kirkpatrick et al. 1983; Press et al. 2007) to retrieve chlorophyll concentration, absorption coefficient for dissolved and detrital material, $a_{dg}(443)$, and the particulate backscattering coefficient, $b_{bp}(443)$, from ocean color radiometry. Similarly, Salinas et al. (2007) used the native simulated annealing procedure (Kirkpatrick et al. 1983) to derive $a_{dg}(440)$, $b_{bp}(550)$, and the absorption coefficient of phytoplankton, $a_{phy}(440)$. Slade et al. (2004) and Zhan et al. (2003) used particle swarm optimization and genetic algorithms, respectively (both global optimization methods) to derive $a_{phy}(440)$, $a_{dg}(440)$, and $b_{bp}(550)$ from ocean color radiometry of optically deep waters.

Table 1. Acronyms and symbols and their definitions.

Acronym	Definition
LM	Levenberg-Marquardt
HSADS	Hybrid Simulated Annealing-Downhill Simplex
SLM	Standard Levenberg-Marquardt approach
UR-LM	Update-Repeat Levenberg-Marquardt approach
LHS	Latin Hypercube Sampling approach
IOPs	Inherent Optical Properties
HICO	Hyperspectral Imager for the Coastal Ocean
BRUCE	Bottom Reflectance Unmixing Computation of the Environment algorithm
SRF	Spectral response function
r_{rs}	Subsurface remote sensing reflectance
r_{rs}^{M}	Forward modeled subsurface remote sensing reflectance
R_{rs}	Above-water surface remote sensing reflectance
λ	Wavelength
θ_v	Subsurface sensor-viewing zenith angle
θ_w	Subsurface solar zenith angle
$a(\lambda)$	Total spectral absorption coefficient of the water column
$b_b(\lambda)$	Total spectral backscattering coefficient of the water column
$a_w(\lambda)$	Spectral absorption coefficient of pure water
$a^*_{phy}(\lambda)$	Specific spectral absorption coefficient of phytoplankton
$a^*_{dg}(\lambda)$	Specific spectral absorption coefficient of detritus and dissolved organic matter
$b_{bw}(\lambda)$	Spectral backscattering coefficient of pure water
$b^*_{bp}(\lambda)$	Spectral backscattering coefficient of suspended particulate matter
$\rho^*_i(\lambda)$	Spectral irradiance reflectance of benthic class *i*
P	Absorption coefficient of phytoplankton at 440 nm
G	Absorption coefficient of colored dissolved and detrital matter at 440 nm
X	Backscattering coefficient of suspended particles at 550 nm
H	Geometric depth of the water column
B_i	Bottom albedo at 550 nm of benthic class *i*

The basis behind these global optimization algorithms is a preliminary search of the multi-parameter solution space from which the global minimum is then located. The only disadvantage of these global optimization techniques is the processing time required to invert a single reflectance spectrum. Processing time becomes particularly critical when propagating uncertainty through the inversion-optimization procedure to derive the uncertainty for each retrieved parameter. Huang et al. (2013) demonstrated the application of a hybrid simulated annealing-downhill simplex (HSADS) routine to derive $a_{phy}(440)$, $a_{dg}(440)$, and $b_{bp}(440)$ from simulated and measured R_{rs} with high accuracy. In a comparison between different optimization schemes, Huang et al. (2013) showed that the Levenberg-Marquardt (LM) algorithm was computationally faster (by a factor of 800) than HSADS, and both methods achieved similar inversion results. Indeed the standardized error and root mean square error between the actual and retrieved IOP values obtained from LM was comparable with that obtained from HSADS. However, HSADS produced 47 more valid retrievals (out of 500 retrievals) than the LM algorithm.

An analysis of the propagation of noise caused from sensor and environmental conditions (e.g., atmospheric fluctuations, sea surface state) through the inversion process to the retrieved geophysical parameters has recently been applied to imagery from several satellite platforms (Garcia et al. 2014; Hedley et al. 2012a). In this method, the derived r_{rs} is perturbed multiple times by the addition of spectrally correlated noise of various magnitudes, and inverted to obtain a range of IOPs, depth and bottom albedo values from which the uncertainties are calculated. This is a computationally demanding procedure where each derived r_{rs} is perturbed, for example, twenty times by the sensor-environment spectral noise (e.g., Hedley et al. 2012a). This effectively means that a given satellite image is inverted 20 times that, when combined with the iterative process of an optimization algorithm, can result in potentially large processing times. Consequently, optimization routines that offer high computational efficiency are desired.

The inclusion of spectrally correlated noise taken from the spectral covariance matrix of an imaged homogeneous deep-water region, potentially introduces more local minima to the

multi-parameter solution space. Such minima add more convergence points on which local optimization algorithms may converge. Use of HSADS or any other global optimization algorithms, though desirable, is computationally prohibitive. Thus in this article we investigate two simple and computationally faster methods, the Update Repeat Levenberg-Marquardt (UR-LM) and Latin Hypercube Sampling (LHS) that guide the LM algorithm to the optimum (if not global) minimum. Here the optimum minimum refers to the minimum with the lowest cost function found during the initial search of parameter space. The UR-LM locates the optimum minimum by taking a finite step away from a local minimum and discerning whether the optimization returns to the same minimum or one with a lower cost function. The UR-LM repeats this procedure if the latter occurs, until either the same minimum is converged to or the number of repeats exceeds ten. The LHS method on the other hand, locates local minima from a wide variety of initial guesses. The local minimum with the lowest cost function is then defined as the optimum. We adopted the LM algorithm as implemented in MPFIT (in C language; Markwardt 2009) that allows for upper and lower bounding constraints. Unlike the LM algorithm employed by Huang et al. (2013), these constraints eliminate issues dealing with nonphysical retrievals.

The UR-LM and LHS methods are in a sense a common tactic in finding the global minimum when using the LM algorithm (Press et al. 2007). Within this study we apply the UR-LM and LHS optimizations schemes in combination with the semi-analytical shallow water algorithm proposed by Klonowski et al. (2007), to invert a selection of r_{rs} observed by the Hyperspectral Imager for the Coastal Ocean (HICO) and a set of simulated r_{rs} spectra. Both the HICO-derived and simulated r_{rs} were selected/simulated for coastal waters with varying benthic substrates, depths, and in-water optical properties. We show that these two methods: (1) are more computationally efficient, i.e., requiring fewer LM iterations when inverting the noise-perturbed r_{rs} compared with the standard approach where the initial guesses are arbitrarily set and fixed; (2) provide lower uncertainties and higher accuracies in the presence of spectrally correlated noise compared to the standard approach; and (3) are not affected by changes to the lower bounds in the constrained LM algorithm, unlike the inversions from the standard approach.

Methods and data

Shallow water model

The semi-analytical Bottom Reflectance Un-mixing Computation of the Environment algorithm, BRUCE (Klonowski et al. 2007), was used to retrieve water column inherent optical properties (IOPs), geometric depth, and key benthic substrates from both simulated and satellite-derived hyperspectral r_{rs}. Klonowski et al. (2007) and Fearns et al. (2011) extensively describe the forward model of the BRUCE algorithm; briefly, the r_{rs} is modeled as a function of the absorption (a) and backscattering coefficients (b_b) of the water column, the geometric depth (H), the bottom reflectance (ρ) and the sun-sensor viewing geometries (Lee et al. 1999),

$$r_{rs}(\lambda;\, a,\, b_b,\, H,\, \rho) \approx \left(0.084 + 0.170u(\lambda)\right)u(\lambda) \left(1 - exp\left\{-\left[\frac{1}{cos\theta_w} + \frac{1.03\left(1+2.4u(\lambda)\right)^{0.5}}{cos\theta_v}\right]\left(a(\lambda)+b_b(\lambda)\right)H\right\}\right) + \frac{\rho(\lambda)}{\pi}\exp\left\{-\left[\frac{1}{cos\theta_w} + \frac{1.04\left(1+5.4u(\lambda)\right)^{0.5}}{cos\theta_v}\right]\left(a(\lambda)+b_b(\lambda)\right)H\right\} \quad (1)$$

$$u(\lambda) = \frac{b_b(\lambda)}{a(\lambda)+b_b(\lambda)} \quad (2)$$

where θ_v and θ_w are the subsurface sensor-viewing zenith and solar zenith angles, respectively. The spectral absorption and backscattering coefficients are themselves functions of the following: (1) the absorption coefficient of phytoplankton at 440 nm, P; (2) the absorption coefficient of colored dissolved and detrital matter at 440 nm, G; and (3) the backscattering coefficient of suspended particles at 550 nm, X, as given by Lee et al. (1999)

$$a(\lambda) = a_w(\lambda) + Pa^*_{phy}(\lambda) + Ge^{-0.015(\lambda-440)} \quad (3)$$

$$b_b(\lambda) = b_{bw}(\lambda) + X\left(\frac{550}{\lambda}\right) \quad (4)$$

where $a_w(\lambda)$ and $b_{bw}(\lambda)$ are the spectral absorption and backscattering coefficients of pure water respectively, and $a^*_{phy}(\lambda)$ is the specific absorption coefficient of phytoplankton normalized to a value of 1.0 at 440-nm. The exponent in Eq. 3 parameterizes the spectral shape of the absorption coefficient of colored dissolved and detrital matter, $a^*_{dg}(\lambda)$. In BRUCE (Klonowski et al. 2007) the net benthic albedo, $\rho(\lambda)$, is expressed as a linear combination of the albedos of three key benthic substrates (typically sediment, seagrass, and brown algae),

$$\rho(\lambda) = \sum_{i=1}^{3} B_i(550\ nm)\rho^*_i(\lambda) \quad (5)$$

where B_i is the albedo at 550 nm and $\rho^*_i(\lambda)$ is spectral irradiance reflectance normalized to a value of 1.0 at 550 nm for the i^{th} benthic class respectively. Both $\rho_i(\lambda)$ and the number of benthic classes can be varied depending on the likely benthos present in the region-of-interest. For HICO imagery of Shark Bay, Western Australia, the bottom albedo was expressed as a linear mix of sand and mixed seagrass (50% *Posidonia australis* and 50% *Amphibolis antartica*) whereas sand, *Posidonia* sp. (seagrass), and *Sargassum* sp. (brown macroalgae) were used for the simulated hyperspectral dataset.

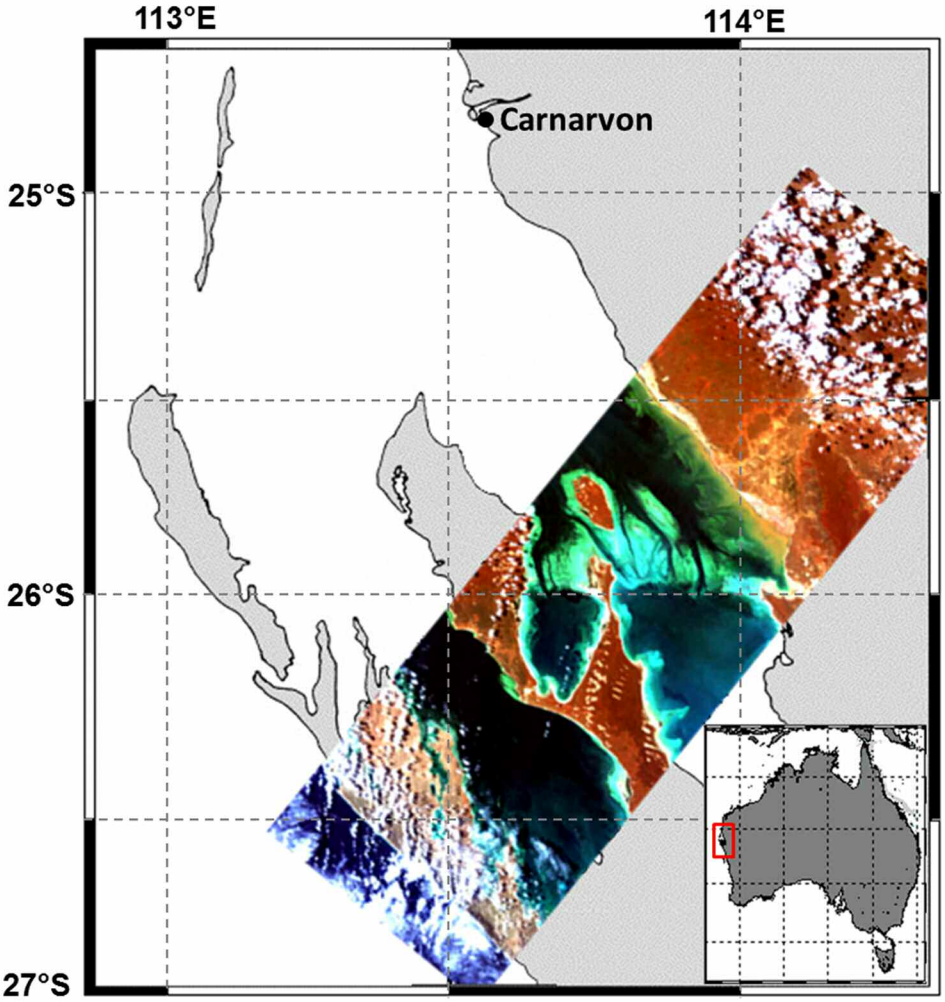

Fig. 1. Map of Shark Bay, Western Australia, Australia, with HICO-derived R_{rs} pseudo true color imagery captured on 14 Dec 2011.

Hyperspectral data and optimization

Hyperspectral satellite imagery

The HICO sensor aboard the International Space Station captured a spectral image of Shark Bay (see Fig.!1), Western Australia, on 14 Dec 2011. The HICO image data provided by the Oregon State University were at-sensor calibrated top-of-atmosphere radiances. These image data were atmospherically corrected using Tafkaa 6S (Gao et al. 2000) to obtain surface remote sensing reflectance (R_{rs}). Here, the aerosol and atmospheric models were set to "maritime" and "mid-latitude summer," respectively. The Tafkaa 6S inputs for aerosol optical thickness at 550 nm, vertical column water vapor and ozone concentrations were obtained from a coincident MODIS image of Shark Bay. Sun-glint and air-water interface corrections were performed on a per-pixel basis to obtain r_{rs} imagery, from which the improved optimizations of the BRUCE algorithm (Klonowski et al. 2007) were tested and compared. Further details on the Shark Bay study site as well as atmospheric, sun-glint, and air-water corrections are given in Garcia et al. (2014). Note that HICO imagery was obtained through the Oregon State University, College of Earth, Ocean, and Atmospheric Sciences, HICO web portal (hico.coas.oregonstate.edu).

Simulated spectra from forward modeling

A total of 4375 simulated hyperspectral r_{rs} spectra of various IOP combinations, depths, bottom types and bottom type mixtures were generated via the BRUCE algorithm's forward model (Eq. 1). These modeled r_{rs} spectra were then convolved with HICO's relative spectral response functions (SRF), using a full width at half maximum of 5.1 nm (Gao et al. 2012) for each band. The resultant simulated r_{rs} dataset therefore had the same spectral resolution and wavelengths as the HICO sensor. The input parameters used to simulate the 4375 HICO r_{rs} are displayed in Table!2 where the range of values shown are similar to those used by Klonowski et al. (2007) in validating the BRUCE algorithm. Here, however, the sensor viewing and solar zenith angles were kept constant at 6.3° and 45.2°, respectively. These angles were used to match the sensor and solar angle geometries of the HICO Shark Bay image from

Table 2. The set of input model parameters used to generate the 4375 simulated HICO r_{rs} spectra via forward modeling. A viewing angle of 6.3° from nadir and a solar zenith angle of 45° were used.

BRUCE model parameter	Value
a_{φ}(440 nm), P (m^{-1})	0.01, 0.03, 0.05, 0.07, 0.10
a_{dg}(440 nm), G (m^{-1})	0.01, 0.1, 0.25, 0.35, 0.50
b_{bp}(550 nm), X (m^{-1})	0.006, 0.010, 0.03, 0.07, 0.10
Depth, H (m)	1, 3, 6, 11, 20
Benthic substrate albedo, B_i (550 nm)	Sand, B_{sand} = 0.227
	Posidonia sp., $B_{seagrass}$ = 0.053
	Sargassum sp., B_{algae} = 0.033
	Mixture 1: 50% sand (B_{sand} = 0.113), 50% *Posidonia* sp. ($B_{seagrass}$ = 0.026)
	Mixture 2: 50% sand (B_{sand} = 0.113), 50% *Sargassum* sp. (B_{algae} = 0.016)
	Mixture 3: 50% *Posidonia* ($B_{seagrass}$ = 0.026); 50% *Sargassum* sp. (B_{algae} = 0.016)
	Mixture 4: 33.3% sand (B_{sand} = 0.076), 33.3% *Posidonia* sp. ($B_{seagrass}$ = 0.018) and 33.3% *Sargassum* sp. (B_{algae} = 0.011)

which spectral noise was extracted and added to the simulated r_{rs} spectra.

One of the aims of this article is to gauge the accuracy of the UR-LM and LHS methods in the presence of real environmental and sensor noise. Such noise not only should account for instrumental noise but also environmental noise produced from atmospheric variability, sun-glint, sky radiance, and the effects of the air-to-water interface present in image data of aquatic systems. To this end, an estimate of the magnitudes and spectral characteristics of such noise were obtained from the HICO r_{rs} image of Shark Bay captured on 14 Dec 2011. The procedure of extracting spectrally correlated noise from the image data and adding it to the r_{rs} (simulated or sensor-derived) is explained in the following section. Here, spectrally correlated noise of varying magnitudes and shapes where added to each simulated r_{rs} spectrum to obtain 100 noise-perturbed r_{rs} spectra. These were then inverted using (i) the standard LM (SLM), (ii) UR-LM, and (iii) LHS implementations of the BRUCE algorithm.

Optimization and uncertainty propagation

As alluded previously, two datasets were used within this study: (1) the HICO-derived r_{rs} image data, and (2) the simulated r_{rs} dataset that mimics the spectral resolution of the HICO sensor (henceforth referred to as simulated r_{rs} dataset). In both datasets, the constrained nonlinear Levenberg-Marquardt (LM) algorithm (Marquardt 1963; Markwardt 2009) was used to derive the model parameters P, G, X, H, B_{sand}, and $B_{seagrass}$. For the simulated r_{rs} dataset, B_{algae} was additionally derived. With this approach we could observe the effect of the SLM, UR-LM, and LHS optimization implementations on the 'best case' simulated r_{rs} data and on 'real world' HICO-derived r_{rs} data. To ensure spectral consistency between the forward modeled r_{rs}^{M} and the HICO-derived and simulated r_{rs} data, the optically active spectral coefficients within the BRUCE algorithm (a_{pw}, a^{*}_{dg}, a^{*}_{phy}, b_{pw}, b^{*}_{bp}, and ρ^{*}_{i}) were convolved with HICO's relative SRFs.

The uncertainties of the derived geophysical parameters were estimated by the noise propagation technique developed by Hedley et al. (2010, 2012a) that takes into consideration both sensor and environmental noise. Note that this propagation technique does not take into account uncertainties caused by differing spectral shapes of IOPs as done in Wang et al. (2005). The uncertainty of each model parameter was determined in the following manner: (i) the spectral covariance matrix, C_{rrs}, of a homogeneous deep-water region was computed from the HICO-derived r_{rs} image of Shark Bay, 14 Dec 2011; (ii) the spectral noise term, δr_{rs}, was then computed as the dot product between an n-band amplitude vector and the Cholesky decomposition matrix, L_{rrs}, of C_{rrs}; (iii) δr_{rs} was then added to the r_{rs} to generate a noise-perturbed spectrum, r_{rs} + δr_{rs}; (iv) steps (ii) and (iii) were repeated to generate a set of m noise-perturbed spectra that were inverted to obtain a set of m optimized model parameters (P, G, X, H, B_{sand}, etc.). The standard error and average from this set were taken as the uncertainty and retrieved value, respectively. Note that (a) the values of the n-band amplitude vector are normally distributed random numbers ($\mu = 0$, $\sigma = 1$) and represent the magnitude of the spectrally correlated noise; (b) the L_{rrs} matrix, which was kept constant throughout the procedure, contains information on the spectral variance of each band and how the spectral bands covary, and (c) the number of m noise-perturbed spectra varied for the two datasets. For the HICO-derived r_{rs} image data m was set to 3000, whereas m = 100 for the simulated r_{rs} dataset. Recall that the HICO-derived r_{rs} dataset underwent atmospheric/sun-glint/air-water interface corrections that add spectral artifacts to r_{rs}. These artifacts introduce more minima to the solution space, and thus m was set to 3000 to observe all the possible convergence points.

The SLM, UR-LM, and LHS implementations of the BRUCE model were tested on four pixels from the HICO-derived r_{rs} image and the set of noise perturbed, simulated r_{rs} spectra. The four pixels selected from the HICO image—based on pseudo

true color imagery and previous benthic surveys (Walker et al. 1988)—have the following geometric depths and benthic substrates: Pixels *A* and *B* are shallow water pixels whose substrates are dominated by bright sediment and seagrass, respectively; *C* is a quasi-deep water pixel with a sandy bottom, and *D* is an optically deep water pixel. The r_{rs} of these four pixels underwent the uncertainty propagation technique described above using the three implementations of the BRUCE model.

The lower bounds of the derived IOPs, geometric depth, and bottom albedos were set to slightly negative values for the constrained LM optimization. This concept follows Werdell et al. (2013) who allowed the range of valid IOP retrievals to be slightly negative to account for noise in the inverted r_{rs} spectrum. Preliminary analysis showed that the bottom albedo coefficients typically produced uncertainties in excess of 40%, and hence the need for more relaxed upper and lower bounds.

$$\begin{aligned} -0.10a_w(490nm) &< P < 2\ m^{-1} \\ -0.10a_w(490nm) &< G < 2\ m^{-1} \\ -0.10b_w(550nm) &< X < 2\ m^{-1} \\ -0.05\ m &< H < 40\ m \\ -0.40\rho_i(550\ nm) &< B_{seagrass}, B_{sand}, B_{algae} < 1.4\rho_i(550\ nm) \end{aligned} \quad (6)$$

Optimizing initial guess

An initial guess for each model parameter is required to initiate the LM optimization. Preliminary investigations showed that the LM algorithm converges to different local minima when the optimization is seeded with different initial guesses. The LHS and UR-LM methods (see flowchart in Fig.!2) that search for the initial guess that guides the LM to the optimum, if not global, minimum are presented.

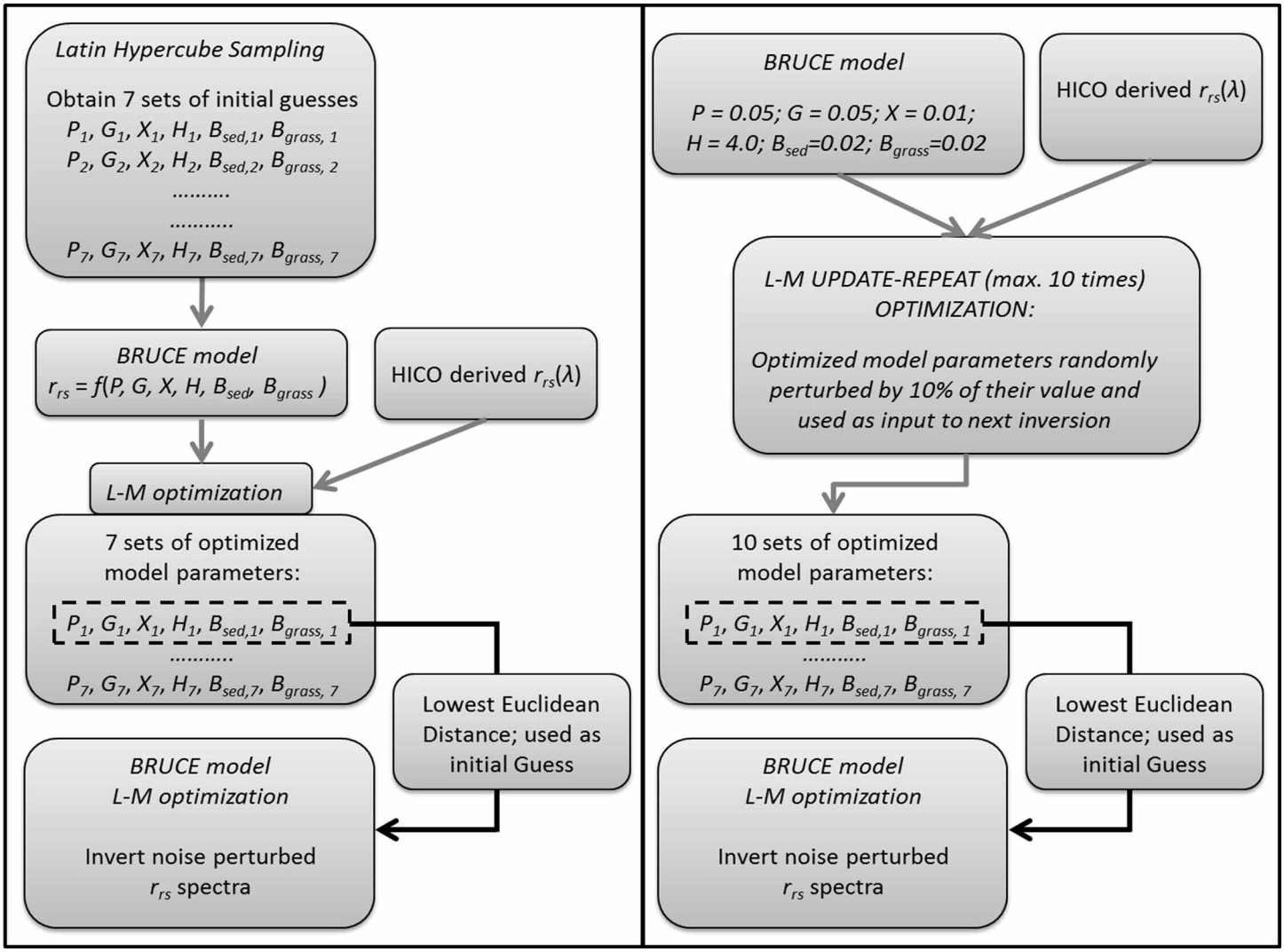

Fig. 2. Flow chart of the Latin Hypercube Sampling (left panel) and Update-Repeat LM optimization (right panel) techniques.

Latin hypercube sampling

Latin hypercube sampling (LHS) is an efficient sampling strategy used to sample the parameter space for an optimal, yet minimal set of initial guess parameters. LHS is an alternative method to simple random sampling, and where the selected samples are guaranteed to cover the full range of variability in the data. The LHS routine has been described extensively by Helton and Davis (2003), Huntington and Lyrintzis (1998), and a step-by-step implementation given by Wyss and Jorgensen (1998). Here, the LHS was used to obtain seven sets of initial guesses,

$$LHS\ Guess = \begin{Bmatrix} P_1 & G_1 & X_1 & H_1 & B_{sed1} & B_{grass1} \\ P_2 & G_2 & X_2 & H_2 & B_{sed2} & B_{grass2} \\ .. & .. & .. & .. & .. & .. \\ P_7 & G_7 & X_7 & H_7 & B_{sed7} & B_{grass7} \end{Bmatrix} \quad (7)$$

where each set was used to seed the inversion of the HICO-derived and simulated r_{rs} spectrum. The set that generated the lowest Euclidean distance was used to seed the inversions of the noise perturbed r_{rs} spectra. For a given spectral image or spectral dataset, obtaining the seven sets of initial guesses (Eq. 7) is only performed once at the start. These initial guesses are then reused throughout the processing to find the optimum initial guess.

Although simple random sampling could have been used to sample the parameter space for initial guesses, it has the following drawbacks: (1) it can potentially exclude sub-ranges of model parameters that have low probability of occurring but have significant impacts on the model output, and (2) would require a large number of samples to effectively sample all of the model parameters' sub-ranges (Helton and Davis 2003). LHS overcomes this by specifying the sub-ranges (or sub-sets) of the model parameter from which one random sample is selected (Helton and Davis 2003; Press et al. 2007). The sub-ranges are selected based of equal probability of the parameters' probability distribution function (PDF). Here, each model parameter was assumed to have a normal PDF bounded by the imposed optimization constraints. With exception, the depth parameter was assumed to have a normal PDF whose mean and standard deviation were 9.5 m and 2.5 m, respectively. The LHS routine of the model parameters in BRUCE followed the program created by Sandia National Laboratories (Wyss and Jorgensen 1998).

Update-Repeat LM optimization (UR-LM)

In the update-repeat LM method, the model parameters that are derived from the optimization process, which represent the solution at a local or global minimum, are randomly perturbed by a finite amount and used to seed a subsequent optimization. This process is continued until either the LM algorithm converges to a minimum with a Euclidean distance of $\leq 1.0 \times 10^{-5}$ or a set number of perturbations have elapsed. This procedure is as follows: an initial inversion of the sensor-derived (or simulated) r_{rs} spectrum is performed with the standard set of LM initial guess values (Eq. 8). If within the first inversion the LM optimization achieved a Euclidean distance $\leq 1.0 \times 10^{-5}$, then the optimized values of the model parameters are used to seed the inversions of the (same) set of noise-perturbed r_{rs} spectra. If, however, the Euclidean distance of the initial inversion was greater than 1.0×10^{-5}, then the optimized values of the model parameters are randomly perturbed by 10% of their value and used as the initial guess for a subsequent inversion of r_{rs}. This perturbation/inversion step is repeated until either the Euclidean distance falls below 1.0×10^{-5} or the number of repetitions occurs more than 10 times. In the latter case, the set of optimized values that generated the lowest Euclidean distance were used as the initial guess for the optimization of the set of noise perturbed spectra. For ease of interpretation, a flowchart of both the LHS and UR-LM methods are presented in Fig. 2.

Assessment

Inverting measured hyperspectral data

Fig.!3 (left panel) shows 3000 noise-perturbed r_{rs} spectra for each of the four pixels (*A*, *B*, *C*, and *D*) selected from HICO imagery of Shark Bay, 14 Dec 2011. Each of these noise-perturbed spectra underwent inversion using the BRUCE algorithm with SLM optimization to derive 3000 optimized values for each model parameter. In the standard algorithm as implemented by Klonowski et al. (2007), the initial guess values were arbitrarily set to

$$P = 0.05; G = 0.05; X = 0.01; H = 4.0; \\ B_{sediment} = 0.02;\ B_{seagrass} = 0.02 \quad (8)$$

The results for this set of inversions using these seed values are presented in Fig.!4 which shows the five different retrieved model parameters *P*, *G*, *X*, B_{sand}, and $B_{seagrass}$, as well as the Euclidean distance plotted against the retrieved depth, *H*, for the inversions of Pixel *A* (HICO image row 1082, column 317).

The inversion results in Fig. 4 show that two distinct solution groups exist at three very different retrieved depths. Group 1, highlighted red in Fig. 4, predominantly had Euclidean distances $< 1.0 \times 10^{-4}$ with retrieved depths between 0.59–0.62 m, and Group 2 had an average Euclidean distance of 3.0×10^{-3} with retrieved depths between 10–13 m. Note, a small set of outliers were also retrieved existing at depths greater than 25 m (see Fig. 4). Groups 1 and 2 represent very different retrieved IOPs, depth, $B_{sediment}$, and $B_{seagrass}$. Table!3 provides an overview of the mean values and uncertainties of each parameter based on the results of the inversions displayed in Figs. 4, 5, and 6. The points displayed in Fig. 4 are presented in the column labeled "SLM BRUCE" in Table 3 for each of the four test pixels selected from the HICO image.

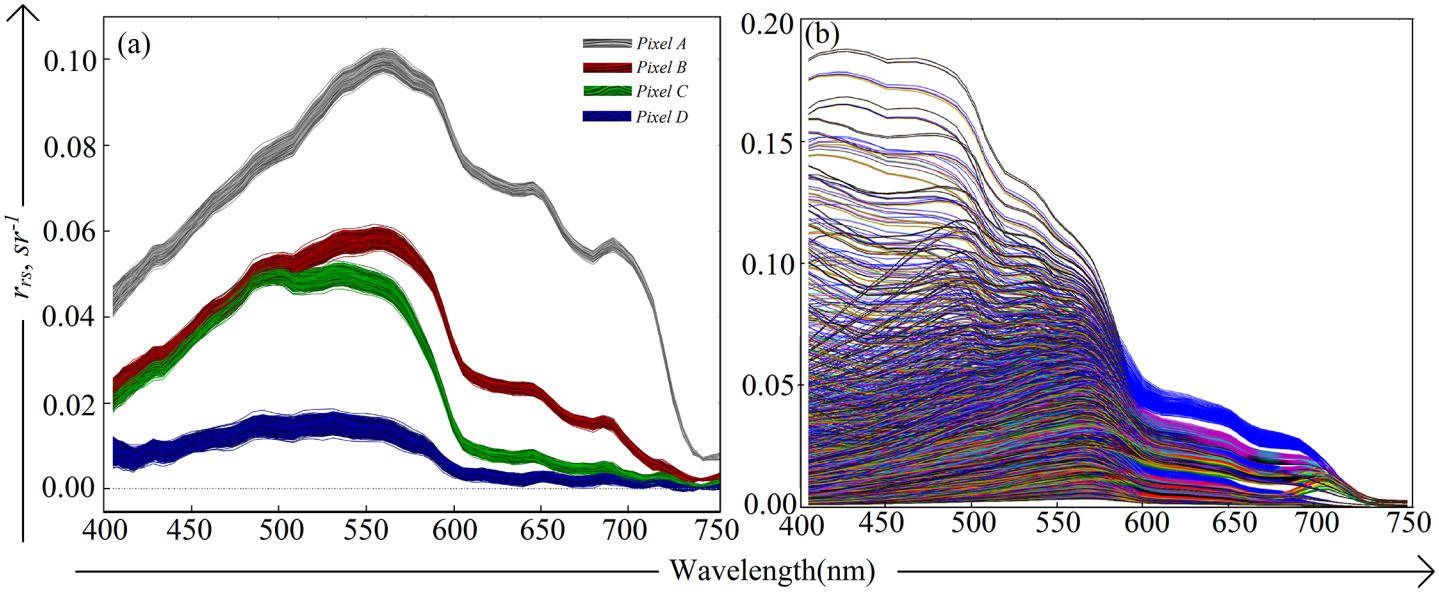

Fig. 3. (a) Tafkaa-6S atmospherically corrected and deglinted, noise-perturbed r_{rs} of pixels A (row 1082, col 317), B (row 1083, col 212), C (row 1031, col 210), and D (row 1200, col 445). Note that 3000 noise-perturbed r_{rs} spectra were generated and shown for each of these four HICO pixels. (b) The 'noise-free' simulated HICO r_{rs} dataset.

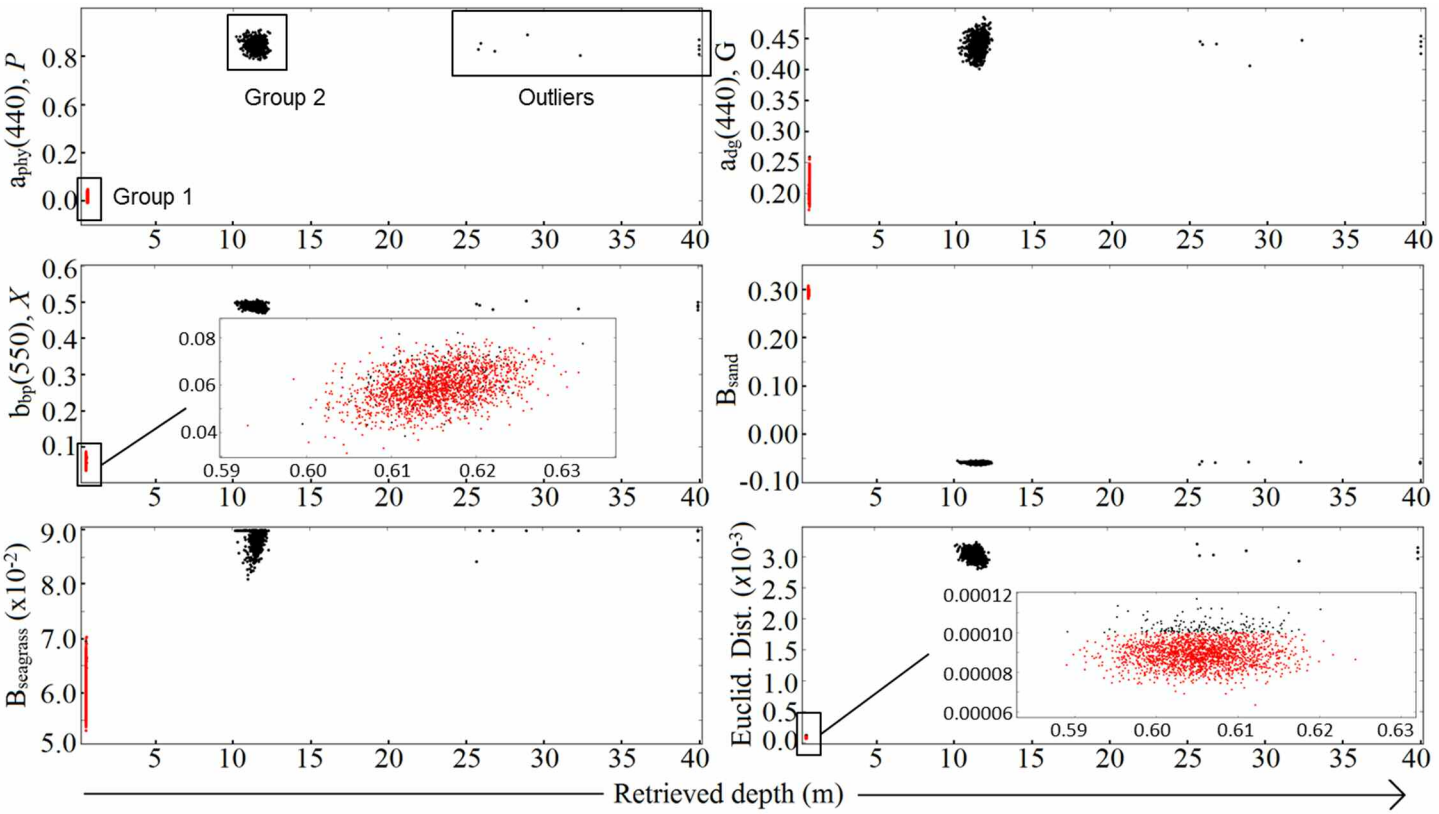

Fig. 4. Retrieved BRUCE model parameters versus retrieved depth for the 3000 noise perturbed r_{rs} spectra of HICO pixel A (row 1082, col 317) using SLM optimization. The seed guess parameters were arbitrarily set. The red dot points are those retrievals whose inversion obtained a Euclidean distance $< 1.0 \times 10^{-4}$.

Table 3. A comparison between the mean and relative standard deviations of the retrieved model parameters, average Euclidean distance, and total number of iterations obtained from the SLM, UR-LM, and LHS implementation of the BRUCE model. Presented are the retrieved model parameters from the four pixels in the HICO image of Shark Bay, 14 Dec 2011.

Pixel type	SLM BRUCE	UR-LM BRUCE	LHS BRUCE
Shallow, sediment substrate (A)			
P (m^{-1})	0.223 ± 134.29%	0.012 ± 77.15%	0.012 ± 77.96%
G (m^{-1})	0.288 ± 37.25%	0.212 ± 5.36%	0.213 ± 5.46%
X (m^{-1})	0.203 ± 99.74%	0.060 ± 11.75%	0.061 ± 11.66%
H (m)	4.37 ± 127.81%	0.60 ± 0.83%	0.60 ± 0.86%
$B_{sediment}$	0.176 ± 94.5%	0.294 ± 1.11%	0.294 ± 1.08%
$B_{seagrass}$	0.071 ± 18.56%	0.061 ± 4.27%	0.061 ± 4.28%
Average Euclidean Dist.	1.11×10^{-3}	9.05×10^{-5}	9.04×10^{-5}
Total Number LM iterations	100,278	31,529	31,596
Shallow, seagrass substrate (B)			
P (m^{-1})	0.020 ± 75.27%	0.025 ± 40.35%	0.026 ± 39.4%
G (m^{-1})	0.254 ± 17.97%	0.269 ± 5.62%	0.269 ± 6.04%
X (m^{-1})	0.080 ± 17.0%	0.084 ± 6.13%	0.084 ± 6.25%
H (m)	1.81 ± 30.89%	2.06 ± 4.6%	2.06 ± 4.55%
$B_{sediment}$	0.152 ± 15.69%	0.159 ± 12.64%	0.159 ± 13.64%
$B_{seagrass}$	0.001 ± 1882.15%	–0.003 ± 396.64%	–0.003 ± 405.57%
Average Euclidean Dist.	1.0×10^{-3}	5.83×10^{-5}	5.81×10^{-5}
Total Number LM iterations	63,764	33,990	33,735
Quasi deep, sediment substrate (C)			
P (m^{-1})	0.015 ± 37.66%	0.015 ± 33.94%	0.015 ± 34.0%
G (m^{-1})	0.106 ± 9.45%	0.105 ± 5.58%	0.105 ± 5.65%
X (m^{-1})	0.027 ± 12.85%	0.027 ± 8.96%	0.027 ± 8.73%
H (m)	5.97 ± 86.42%	5.18 ± 3.08%	5.18 ± 3.13%
$B_{sediment}$	0.361 ± 10.61%	0.361 ± 9.69%	0.361 ± 9.82%
$B_{seagrass}$	0.003 ± 792.87%	0.002 ± 1221.57%	0.002 ± 1148.18%
Average Euclidean Dist.	$5{,}74 \times 10^{-5}$	4.44×10^{-5}	4.43×10^{-5}
Total Number LM iterations	76,675	35,623	35,657
Optically deep (D)			
P (m^{-1})	0.026 ± 72.51%	0.027 ± 70.78%	0.026 ± 70.32%
G (m^{-1})	0.138 ± 15.1%	0.137 ± 15.42%	0.138 ± 15.3%
X (m^{-1})	0.012 ± 15.97%	0.012 ± 15.69%	0.012 ± 15.75%
H (m)	11.90 ± 50.69%	11.61 ± 44.89%	11.50 ± 45.08%
$B_{sediment}$	0.054 ± 220.44%	0.056 ± 208.12%	0.055 ± 207.31%
$B_{seagrass}$	0.021 ± 210.29%	0.020 ± 212.46%	0.021 ± 210.91%
Average Euclidean Dist.	2.11×10^{-5}	2.06×10^{-5}	2.06×10^{-5}
Total number LM iterations	66,383	57,425	57,196

Here, SLM stands for the Standard Levenberg-Marquardt implementation of BRUCE. The results of the SLM for HICO pixel *A* collectively produced high uncertainties including retrieved parameter averages that were larger relative to the UR-LM and LHS approaches (see Table 3).

Arguably one might consider that a given r_{rs} spectrum should have a unique point in retrieved parameter space that generates the lowest possible Euclidean distance. Thus for situations where non-uniqueness is not an issue, one would assume that adding spectral noise to the r_{rs} spectrum would simply create dispersal about this unique point in parameter space rather than dispersals about two or more different minima. Note that in parameter space, the non-uniqueness of the r_{rs} spectrum would represent a situation where two or more local minima exist that have very similar Euclidean distances but very different solutions. For HICO pixel *A* (Fig. 4), each solution cluster has a substantially different Euclidean distance. Thus non-uniqueness was not deemed the cause, but rather the convergence onto two substantially different minima.

Without ground truth data it is unknown which of the two minima in Fig. 4 is representative of the true environmental parameters. However, pragmatically we can assume the mini-

mum with the most realistic solution being the one with the best model fit (i.e., lowest Euclidean distance). In the case of HICO pixel *A* (Fig. 4), this would be Group 1 where the model parameters range between $0.0 < P < 0.05$ m^{-1}, $0.17 < G < 0.26$ m^{-1}, $0.03 < X < 0.08$ m^{-1}, $0.59 < H < 0.62$ m, $0.28 < B_{sediment} < 0.31$, and $0.05 < B_{seagrass} < 0.07$. The depth taken from the nautical chart of Shark Bay, Western Australia, at the approximate area of HICO pixel *A* ranged between 0.3 to 0.4 m (above lowest astronomical tide, LAT). We note that the retrieved depth of 0.6 m was the depth at the time of the HICO overpass, and was not corrected for tide to a chart datum such as LAT. Thus taken into consideration the tide and possible depth offsets caused by atmospheric correction, a retrieved depth of 0.6 m is quite possible.

A method that guides the LM optimization is clearly needed to avoid multiple solution minima so that a true representation of the mean and standard deviation for each retrieved model parameter can be obtained. Although it is possible to perform a post-processing density based cluster analysis to isolate the solution group with the lowest Euclidean distance, it is more ideal (with regards to processing time) to have a robust method that only converges to one minimum. Figs.!5 and!6 present the results of the inversions of HICO pixel *A* using the UR-LM and LHS implementation of the BRUCE model, respectively. In these two methods the inversions show only one group of solutions indicative of the convergence to a single minimum. Moreover, this minimum is the same as Group 1 of Fig. 4, and demonstrates that the UR-LM and LHS methods both guided the LM optimization to the optimal solution (based on lowest Euclidean distance). Indeed the inversions using these methods were considerably more precise; for example, the retrieved depth from the SLM was 5.97 ± 5.16 meters (5.97 m ± 87%, see Table 3) whereas through the UR-LM method the retrieved depth changed to 5.18 ± 0.16 m for HICO pixel *C* (*see* Table 3). Additionally, the IOP retrievals for pixel *A* appear to have been improved with the UR-LM and LHS methods relative to the SLM approach. Recall that pixel *A* is characterized as very shallow with a bright sand substrate, thus the majority of the magnitude of the r_{rs} arises from bottom reflectance. Retrievals of the absorption and backscattering coefficients and the depth, using the SLM for HICO pixel *A* were considerably larger compared with values retrieved using the UR-LM and LHS methods. This implies that the SLM preferentially translates the magnitude of the r_{rs} signal to a higher signal from the water column (i.e., higher backscattering coefficient), and therefore decreases the bottom reflectance signal by both increasing the depth and absorption coefficients. In contrast, the UR-LM and LHS methods avoided

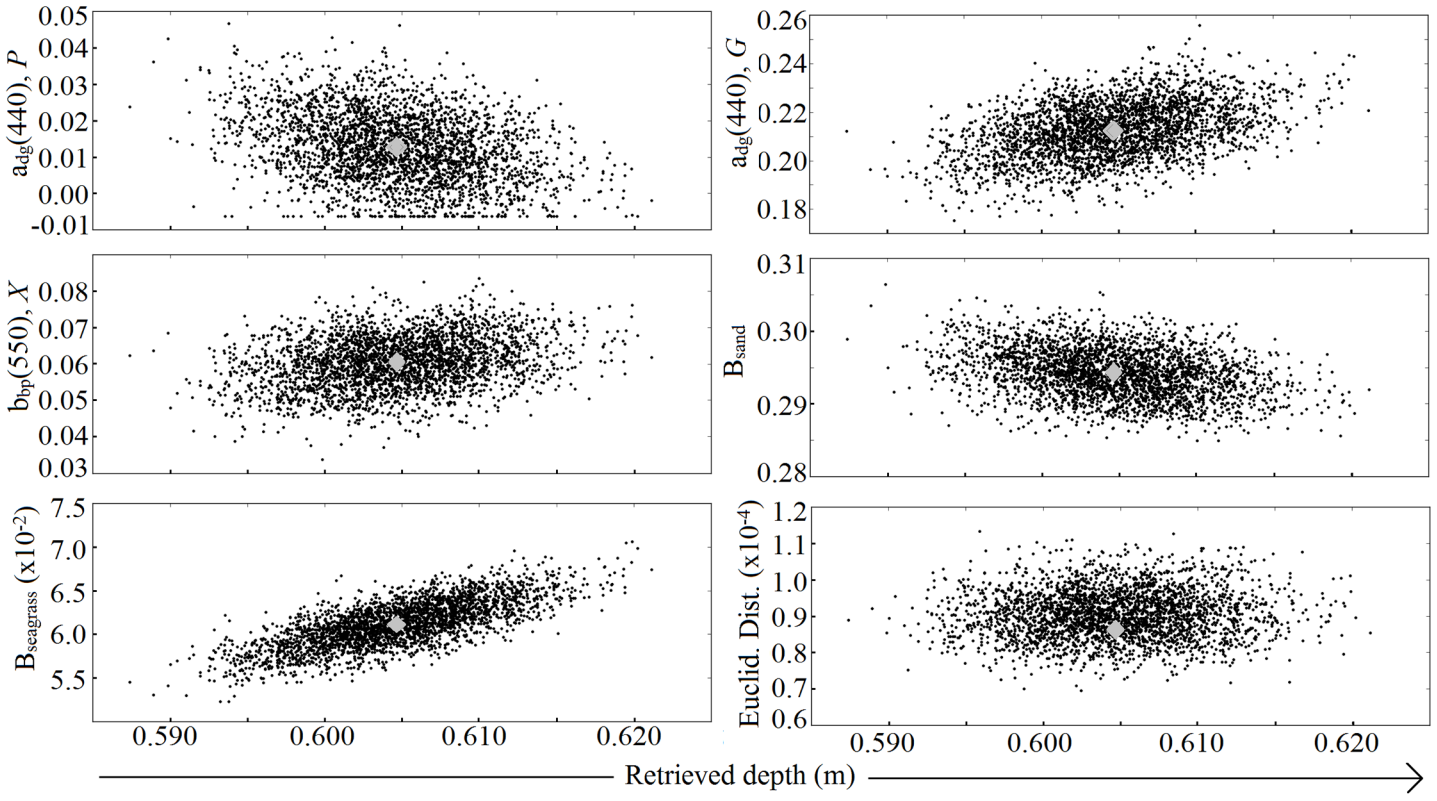

Fig. 5. Retrieved BRUCE model parameters versus retrieved depth for the 3000 noise perturbed r_{rs} spectra of the HICO pixel A (row 1082, col 317). The optimized guess values used to seed the LM optimization were dynamically chosen using the UR-LM method shown as gray diamonds.

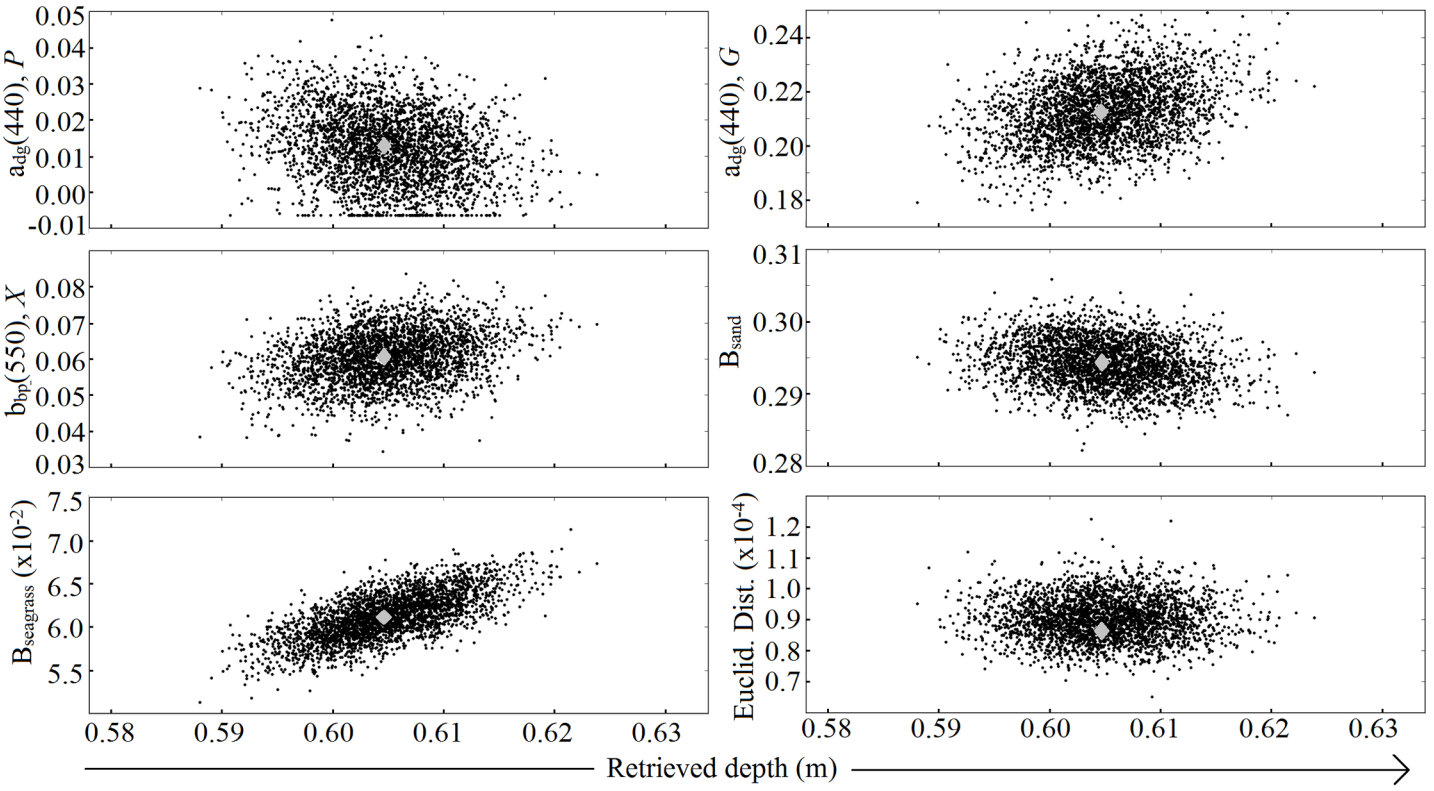

Fig. 6. Retrieved BRUCE model parameters versus retrieved depth for the 3000 noise perturbed r_{rs} spectra of the HICO pixel A (row 1082, col 317). The optimized guess values were dynamically chosen using the LHS method, shown as gray diamonds.

the overcontribution of the water column reflectance, allowing both methods to retrieve a shallower, more realistic depth.

Web Appendix A shows the inversion results of the other HICO pixels (*B*, *C*, and *D*). The basis behind the UR-LM and LHS methods is the selection of an optimized initial set of LM guess parameters that correspond to the lowest minimum found during the initial parameter search. Using this optimized guess to seed the inversion of the noise perturbed r_{rs} spectra generally increases the computational efficiency of the inversions. Here, computational efficiency is defined as the total number of iterations (T_i) that the LM algorithm performed. This enhanced efficiency is presented in Table 3, which compares the retrieved model parameters, average Euclidean distance and number of iterations between the SLM, UR-LM, and LHS BRUCE implementations. For the SLM, T_i accounts for the number of iterations incurred during 3000 spectral inversions, whereas for the UR-LM and LHS, T_i also includes the number of iterations incurred during the search for the optimized initial guess. The results shown in Table 3 indicate that the UR-LM and LHS methods are comparable and at least twice more computationally efficient than the SLM.

Although the UR-LM and LHS methods can yield improved optimizations for optically shallow to quasi-deep pixels, it does not improve the inversion of optically deep-water pixels (see Table 3, HICO pixel *D*). This, however, is due to the BRUCE model attempting to retrieve depth and bottom albedo coefficients from an r_{rs} spectrum that has negligible bottom contribution. It is therefore important to have a method of determining whether a pixels' r_{rs} spectrum relates to deep-water or not (e.g., Brando et al. 2009) and to be able switch between ocean color models such as the Generalized IOP algorithm (Werdell et al. 2013) and a shallow water model such as BRUCE.

Inverting simulated hyperspectral data

An assessment of the sensitivity to noise and accuracy of the retrieved geophysical parameters from the three optimization approaches was carried out by inverting noise-perturbed, simulated r_{rs} spectra. Specifically, the BRUCE model was implemented in a forward sense where a range of values for the model inputs (see Table 2) was used to obtain 4375 modeled r_{rs}. For each of these modeled spectra, the uncertainty propagation technique produced 100 noise-perturbed r_{rs} spectra (i.e., a total of 437,500 spectra) that were inverted to retrieve the uncertainty and average value of the model parameters. Note that we have chosen to use forward modeling rather than relying on radiative transfer numerical models such as Hydrolight (Mobley and Sundman 2000) or PlanarRad (Hedley 2008) to exclude sources of uncertainty from the BRUCE model parameterization. Such uncertainties arise from assumptions made

regarding the bottom albedo, chlorophyll model, phase functions, and sun-sensor viewing geometries. Thus, in this context forward modeling is an ideal situation, because before the addition of spectrally correlated noise the optimization procedures would be expected to produce 100% accuracy between the retrieved and input model parameters.

Figs.!7,!8 and!9 compare the retrieved versus input BRUCE model parameters using the SLM, UR-LM, and LHS optimization methods. Table!4 presents the accuracy, average uncertainty, average retrieved value, and root mean square error (RMSE) between the retrieved and input model parameter for these three methods. The accuracy of the three methods was assessed based on the proportion of retrievals that were within 1% of the input model parameter. Thus, the ideal scenario of 100% accuracy implies that all the retrievals were within 1% of the input model parameter. Here, the average retrieved value (henceforth referred to as centroid) was used to assess how close the retrievals are to the input model value, whereas the RMSE was used as a measure of the scatter the retrievals have about the "true" value

$$RMSE = \left[\frac{\sum_{i=1}^{M} \left(\hat{x}_{i,j} - x_j \right)^2}{M-1} \right]^{1/2} \quad (9)$$

where $\hat{x}_{i,j}$ is the i^{th} retrieval of the j^{th} BRUCE model parameter (P, G, X etc), x_j is the true value of the j^{th} model parameter, and M being the number of retrievals. The normalized RMSE (Eq. 9 divided by the average retrieved value of the scatter) was not used as this tends to very large values as the average retrieved value approaches zero. Here, the optimization method that generated the lowest RMSE, relative uncertainty, and highest accuracy was considered the most optimal. Note that the accuracies presented in Table 4 will be lower when inverting sensor-derived subsurface remote sensing reflectance due to uncertainty in the model parameterization, and potentially erroneous radiometric corrections arising from atmospheric fluctuations and sea surface state (sun-glint and air-water interface).

Figs. 7 to 9 show that in the presence of spectral noise the SLM leads to retrievals that have much greater scatter and variation about the actual (or true) parameter value. This is seen, for example, in the retrievals of the phytoplankton absorption coefficient, P (Fig. 7), where there appears to be little or no correlation between the retrieved and actual values for the SLM. In contrast the results for the UR-LM and LHS show a much improved agreement between input and retrieved values for P. Indeed, the scatter (RMSE) for the majority of the model parameters were consistently greater than the input value for the SLM method. The LHS method has considerably lower RMSE than the SLM method; in fact the LHS method reduced the scatter on average by factors of 5, 56, 194, and 11 for parameters P, G, X, and H, respectively, when compared with the SLM. The UR-LM method on the other hand has only reduced the scatter, on average by factors of 2, 8, 78, and 1.9 for P, G, X, and H, respectively, when compared with the SLM. In addition to the reduced

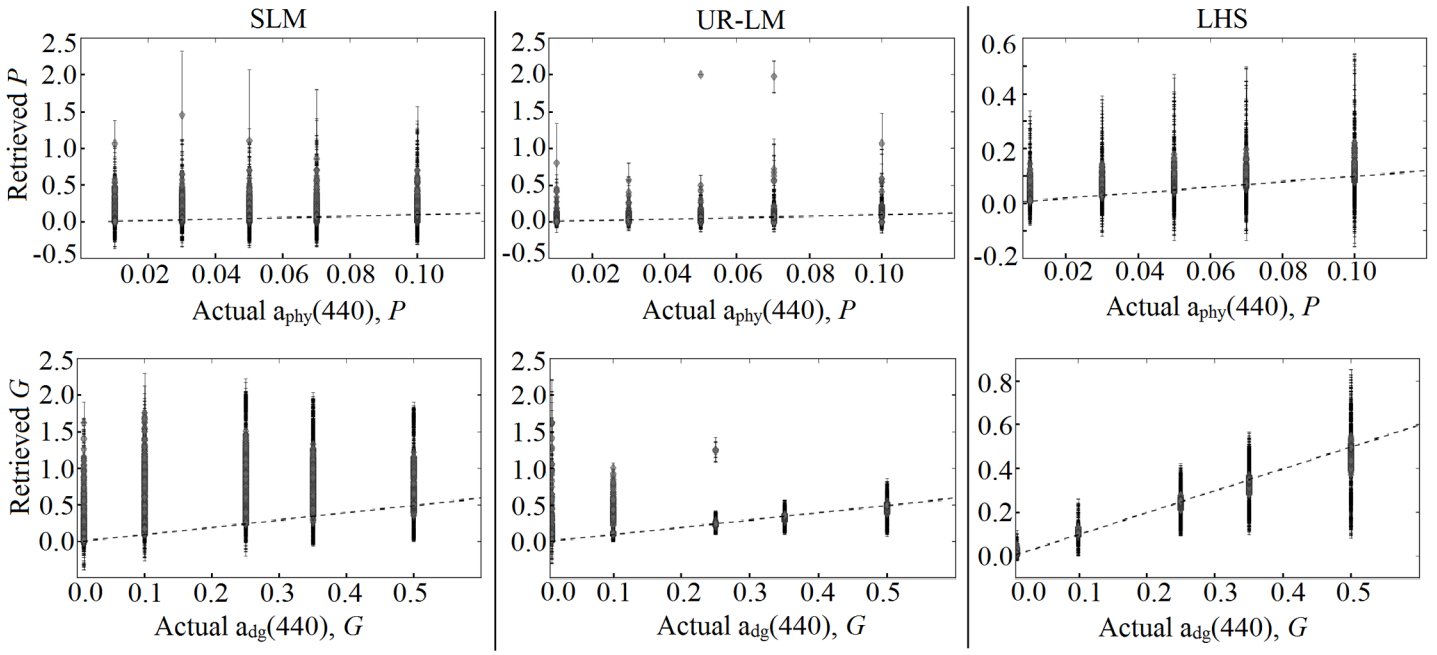

Fig. 7. Inter-comparison between the SLM (left-hand panels), UR-LM (central panels), and LHS (right-hand panels) optimization of the noise-added simulated r_{rs} spectra using the BRUCE model. These graphs show the retrieved versus actual model parameters for P, and G Note: (1) the uncertainty in each retrieval (gray diamonds) are represented as error bars; (2) the dashed line in each graph represents the ideal 1:1 ratio between retrieved and actual.

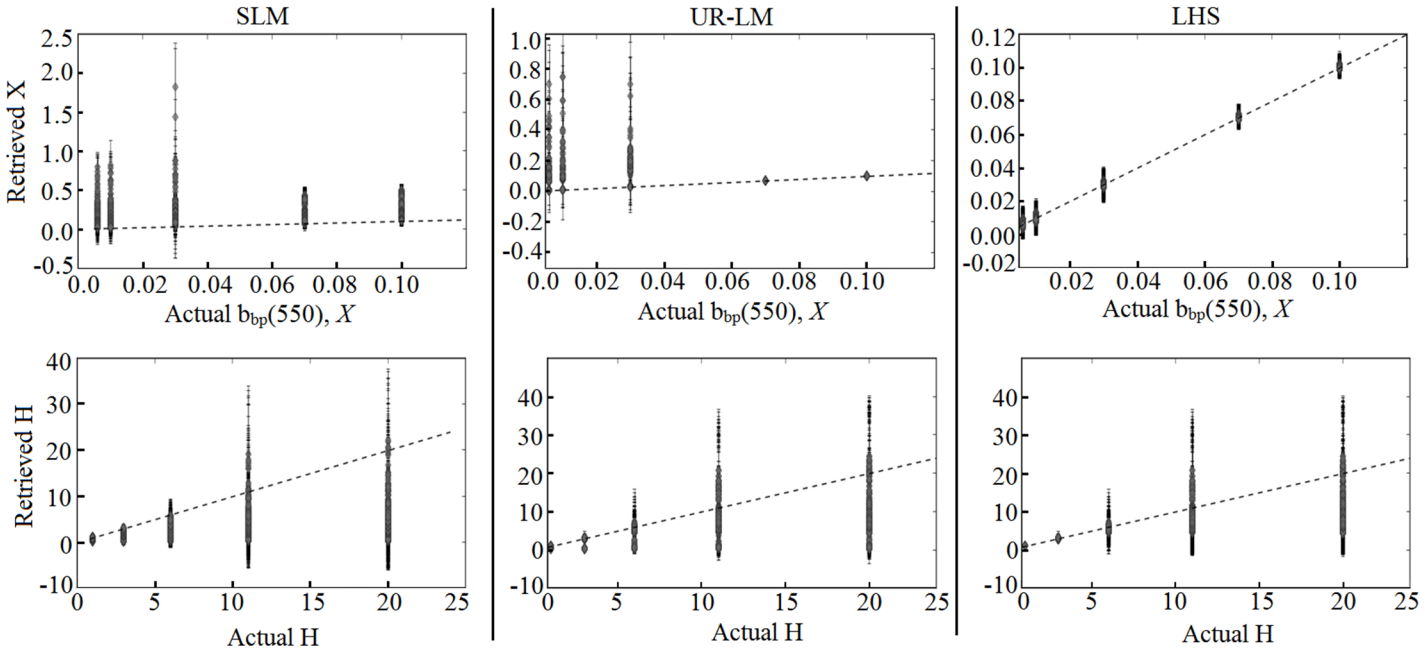

Fig. 8. Intercomparison between the SLM, UR-LM, and LHS optimization of the noise-added simulated r_{rs} spectra using the BRUCE model. These graphs show the retrieved versus actual model parameters for X and H.

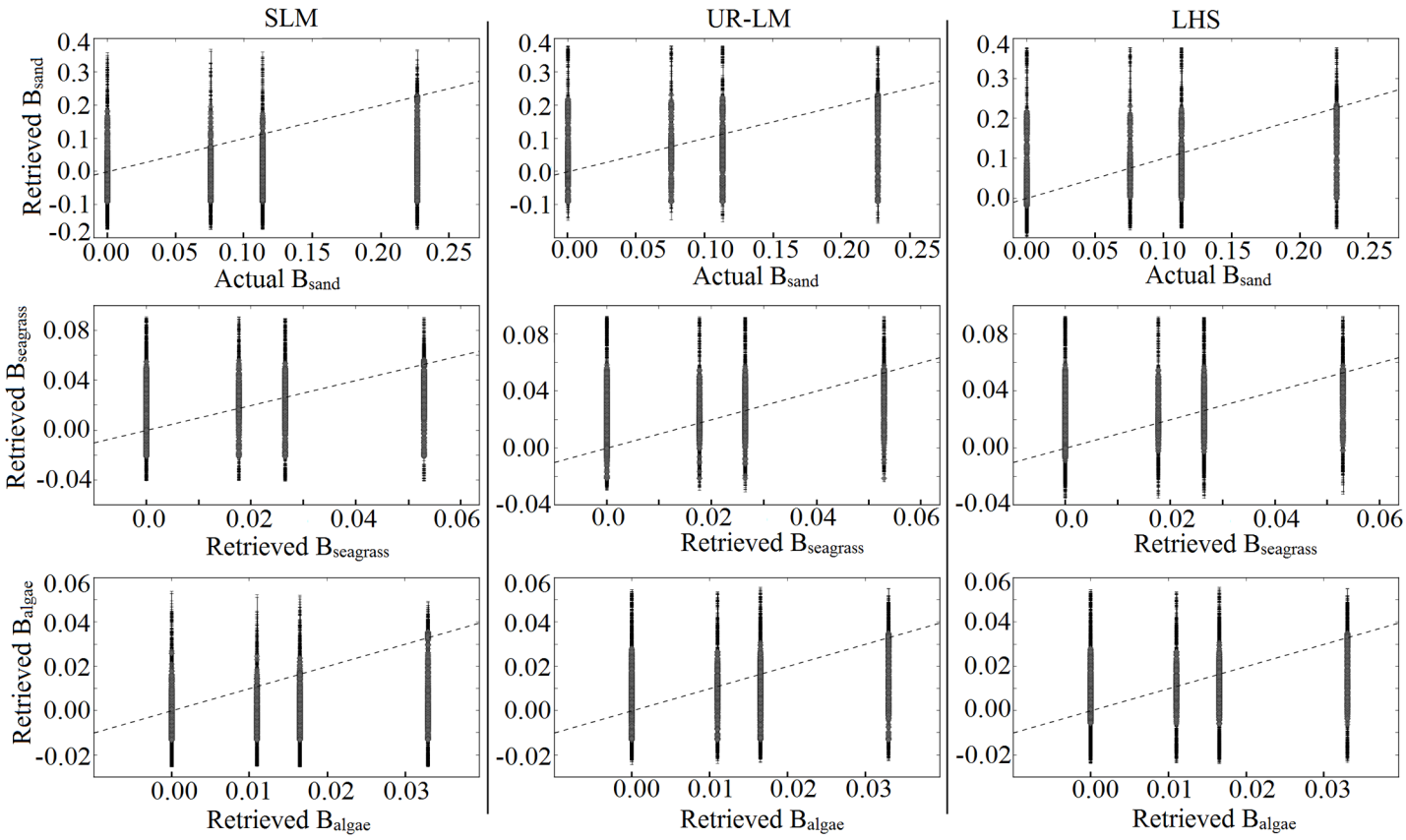

Fig. 9. Intercomparison between the SLM, UR-LM, and LHS optimization of the noise-added, simulated r_{rs} spectra using the BRUCE model. These graphs show the retrieved versus actual model parameters for B_{sand} (top), $B_{seagrass}$ (middle), and B_{algae} (bottom).

Table 4. An intercomparison of the RMSE (scatter), percent accuracy, average relative uncertainty, and average retrieved value for each BRUCE model parameter between the three optimization approaches. Recall that 100% accuracy is ideal as all the retrievals would be within 1% of the input model parameter.

Actual	Average retrieved value (centroid)			Average uncertainty			RMSE			Accuracy (%)		
values	SLM	UR-LM	LHS	SLM	UR-LM	LHS	SLM	UR-LM	LHS	SLM	UR-LM	LHS
P (m^{-1})												
0.01	0.058	0.021	0.019	0.085	0.033	0.030	0.117	0.047	0.023	1.37	4.11	4.69
0.03	0.067	0.034	0.034	0.097	0.038	0.036	0.115	0.037	0.021	1.83	7.77	9.26
0.05	0.078	0.052	0.051	0.107	0.041	0.041	0.108	0.074	0.020	2.06	10.74	13.14
0.07	0.087	0.071	0.067	0.113	0.048	0.045	0.103	0.081	0.018	3.09	13.71	16.11
0.1	0.105	0.097	0.094	0.126	0.055	0.053	0.101	0.049	0.018	4.80	19.77	20.23
G (m^{-1})												
0.01	0.120	0.054	0.008	0.078	0.031	0.007	0.250	0.172	0.004	1.37	7.66	10.63
0.1	0.450	0.138	0.082	0.177	0.027	0.021	0.517	0.153	0.004	2.74	29.37	36.57
0.25	0.669	0.218	0.215	0.362	0.046	0.045	0.544	0.059	0.010	4.57	40.00	40.00
0.35	0.670	0.311	0.312	0.385	0.063	0.064	0.402	0.020	0.020	2.86	37.14	37.26
0.5	0.643	0.475	0.475	0.328	0.093	0.093	0.231	0.040	0.040	5.60	29.71	29.71
X (m^{-1})												
0.006	0.096	0.026	0.006	0.077	0.009	0.004	0.136	0.067	0.001	0.00	2.86	5.83
0.01	0.108	0.030	0.010	0.074	0.009	0.004	0.144	0.070	0.001	0.23	4.34	7.77
0.03	0.154	0.059	0.025	0.088	0.014	0.004	0.177	0.111	0.001	0.80	17.14	24.46
0.07	0.163	0.050	0.050	0.084	0.004	0.004	0.121	0.001	0.001	4.23	46.51	46.51
0.1	0.180	0.082	0.082	0.068	0.004	0.004	0.124	0.001	0.001	7.20	69.94	70.06
H (m)												
1	0.98	0.98	1.00	0.18	0.05	0.04	0.15	0.10	0.01	47.89	85.03	88.69
3	1.59	2.88	3.00	0.98	0.30	0.30	1.62	0.54	0.07	1.71	48.80	51.31
6	2.44	4.58	5.30	2.01	1.37	1.42	3.83	2.00	0.50	0.00	6.63	11.89
11	3.60	4.83	6.21	3.89	4.27	4.69	7.82	5.02	3.22	0.23	0.34	2.29
20	3.75	4.99	6.46	4.35	5.28	6.25	16.55	11.75	9.76	0.00	0.46	0.80
B_{sand}												
0	–0.011	0.017	0.023	0.060	0.056	0.061	0.043	0.054	0.052	0.00	0.00	0.00
0.0757	0.009	0.055	0.067	0.069	0.060	0.065	0.087	0.053	0.034	2.08	12.00	13.44
0.1135	0.018	0.072	0.089	0.073	0.061	0.065	0.116	0.065	0.036	4.48	14.88	17.44
0.227	0.056	0.134	0.156	0.089	0.061	0.065	0.199	0.112	0.072	11.36	24.00	25.12
$B_{posidonia}$												
0	0.014	0.010	0.009	0.020	0.020	0.022	0.022	0.019	0.018	0.00	0.00	0.00
0.0177	0.020	0.018	0.018	0.020	0.021	0.023	0.014	0.011	0.010	3.04	7.84	7.84
0.0265	0.023	0.022	0.023	0.020	0.021	0.023	0.014	0.009	0.009	5.60	9.52	9.92
0.053	0.031	0.034	0.036	0.020	0.021	0.023	0.029	0.019	0.017	8.00	12.48	12.80
$B_{sargassum}$												
0	–0.003	0.003	0.004	0.013	0.014	0.015	0.007	0.008	0.007	0.00	0.00	0.00
0.011	0.000	0.008	0.009	0.013	0.015	0.016	0.013	0.007	0.005	4.00	4.64	4.96
0.0165	0.002	0.010	0.012	0.014	0.015	0.016	0.017	0.009	0.007	4.96	6.40	6.96
0.033	0.007	0.017	0.019	0.015	0.015	0.016	0.029	0.017	0.016	6.56	10.88	12.32

Number of L-M iterations
SLM 42,380,282
UR-LM 13,150,908
LHS 11,132,485

RMSE, the UR-LM and LHS methods have centroids for the IOPs and depth closer to the actual value than the SLM (see Table 4).

Fig.!10 displays density plots of the bias in the downwelling diffuse attenuation coefficient at 490 nm, $K_d(490)$ plotted against bias in depth; and the bias in B_{sand}, $B_{seagrass}$ and B_{algae} versus depth bias, for the SLM and LHS optimization

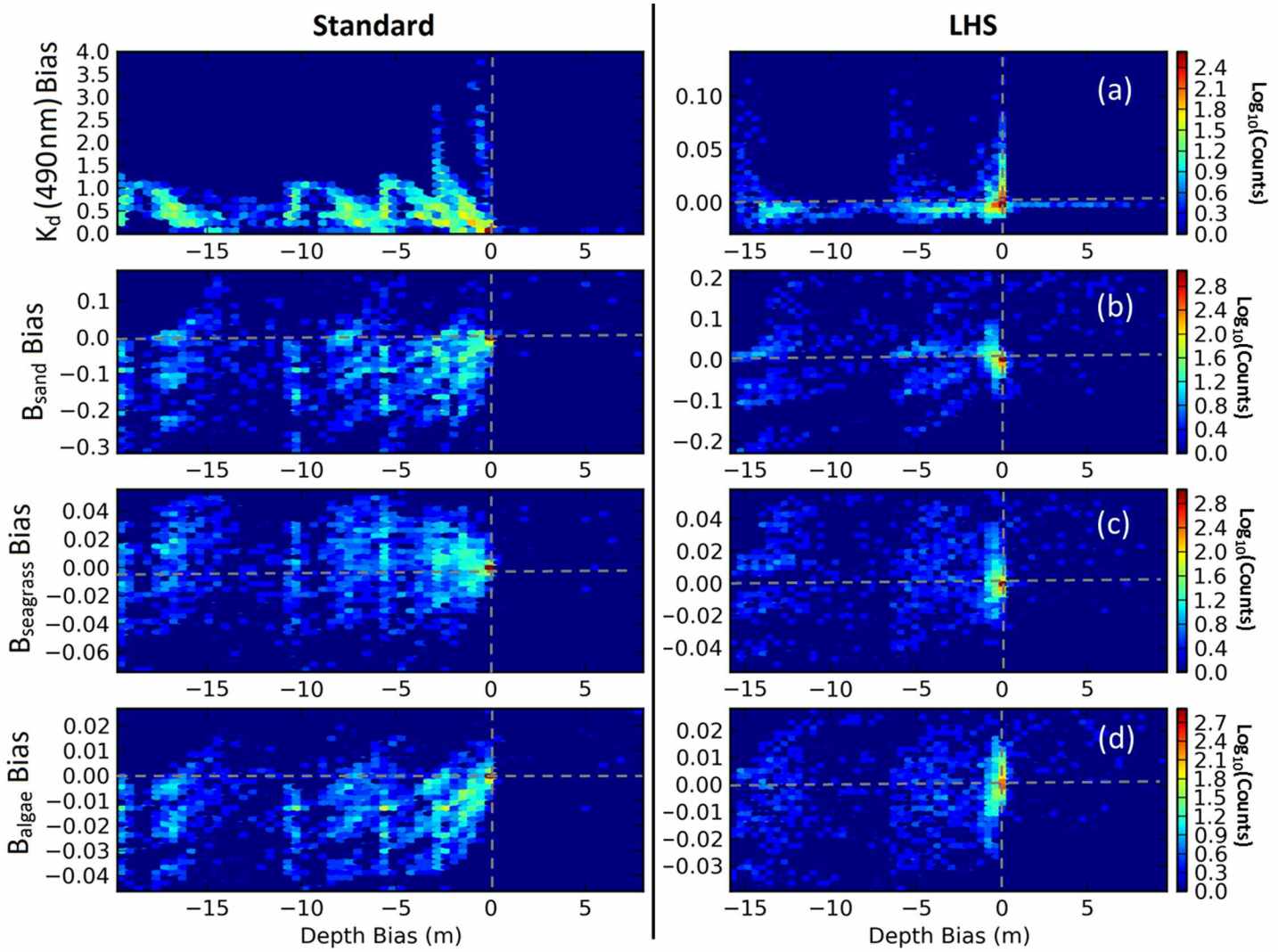

Fig. 10. Density plots of (a) K_d(490 nm) bias versus depth bias; (b) B_{sand} bias versus depth bias; (c) $B_{seagrass}$ versus depth bias, and (d) B_{algae} bias versus depth bias. Each pixel in the density plot has a frequency of occurrence, represented by its color. The left- and righthand panels show the bias obtained using the SLM and LHS optimization methods, respectively.

approaches. The bias was defined as the retrieved minus actual parameter value, thus negative bias represents underestimation and vice-versa for a positive bias. Here, $K_d(490)$ was computed by

$$K_d(490) = \frac{a(490) + b_b(490)}{\cos(\theta_w)} \quad (10)$$

where $a(490)$ and $b_b(490)$ are the absorption and backscattering coefficients of the water column at 490 nm. The retrieved and true values of P, G, and X were used as inputs to Eqs. 3 and 4 to compute $a(490)$ and $b_b(490)$, respectively. Also, θ_w was set to the sub-surface solar zenith angle at the time of the HICO overpass on 14 Dec 2011. The bias in $K_d(490)$ was thus computed by $K_{d,\ retrieved}(490)$ - $K_{d,\ actual}(490)$. The results in Fig. 10 show that the SLM procedure, for the majority of the inversions, simultaneously overestimated $K_d(490)$ and underestimated depth and the bottom albedo coefficients. This implies that the BRUCE model, when initiating the SLM optimization with a fixed initial guess, preferentially underestimates the depth by compensating for a more turbid water column and darker substrate. This is an example of the LM algorithms' inability to move beyond local minima. In the SLM approach the initial guess for depth was 4 m (see Eq. 8), thus as the LM algorithm increased or decreased the depth parameter in the direction of lowest Euclidean distance, it encountered and converged to a local minimum rather than continuing the optimization process toward the global minimum.

When comparing the bias in $K_d(490)$ with the bias in depth (Fig. 10a), the LHS method produced depth retrievals more centered on a bias of zero than the SLM approach. Indeed, the SLM had biases in depth up to –20 m where the $K_d(490)$ bias predominantly ranged between 0 and 1.5 m^{-1}. The LHS

method in contrast, had $K_d(490)$ bias ranging between –0.05 and 0.10 m^{-1}, and a bias in depth that ranged between –15 and 10 m. It should be noted that these large biases in depth of the LHS method had (i) a substantially lower frequency of occurrence (see the color bar in Fig. 10) compared with the SLM method and (ii) were obtained for the inversions of simulated r_{rs} whose input depths were greater than 10 m—as illustrated by the large scatter about these retrieved depths in Fig. 8. This latter result emphasizes the optical depth limit of shallow-water inversion models.

In the LHS method, the depth was still preferentially underestimated though not the extent of the SLM. This is also observed by centroids of the depth retrievals (Table 4), which plateau to around 3 to 4 m for input depths greater than 6 m using the SLM method, whereas the centroids reach 6.48 m using the LHS method. Importantly, the LHS method has improved the bias of $K_d(490)$, which in turn, relates to improved accuracies of the retrieved IOPs over a range of depths—particularly over shallow water where the bottom reflectance can contribute more to the net water-leaving signal than water column optics.

The UR-LM and LHS methods have significantly increased the accuracy of the depth retrievals and indeed the other retrieved parameters. In the SLM approach, the accuracies of retrieved depths greater than or equal to 3 meters are less than 2%. This has increased to accuracies of 51.3%, 11.9%, 2.3%, and 0.80% for retrieved depths of 3, 6, 11, and 20 m respectively using the LHS method. The rapid decline in accuracy and increased scatter about the true value with depth is associated with the exponential nature of light attenuation. At depths greater than 10 m, the bottom contribution to the r_{rs} signal is typically very small, resulting in minor differences between an r_{rs} spectrum at, say 15 m to that at 20 m for the same set of optical conditions. Hence the BRUCE model can converge to a large range of depths (e.g., 15–25 m) without significantly affecting the model fit. Despite these increases in accuracies, the accuracies of the retrieved depths, IOPs, and benthic albedo coefficients are typically less than 50% using the UR-LM and LHS methods, which illustrate the sensitivity of these model parameters to the addition of spectral noise.

Retrievals of the bottom albedo parameters (B_{sand}, $B_{posidonia}$, $B_{sargassum}$) were only marginally improved with the UR-LM and LHS methods. These parameters suffer from very low accuracy (<26%) and precision (>40 % relative uncertainty). For these three methods, the highest accuracies were obtained for bright bottom substrates, where 100%, 50%, and 33% benthic sediment mixtures obtained accuracies of 25%, 17%, and 13%, respectively. These accuracies decreased as the substrate became darker, for instance the accuracy for $B_{sargassum}$ was on average 2% less than that of $B_{posidonia}$. These low accuracies are likely due to the overparameterization of the BRUCE model where non-zero albedo coefficients are always retrieved even if only one benthic type was modeled (despite having set negative lower bounds [$-0.4\rho_i$, see Eq. 6] in the LM optimization). Such accuracies have significant implications to benthic classification when total system noise is incorporated in the analysis. Further work is therefore necessary to improve the accuracies of these bottom albedo coefficients.

We found that changing the lower bounds of the BRUCE model parameters can affect the accuracy, RMSE, and uncertainty of the retrievals dramatically. So much so that when the lower bounds of the IOPs, depth, and bottom albedo coefficients were set to zero, the inversion results using the SLM become similar to the UR-LM and LHS methods (*see* Web Appendix B). However, the UR-LM and LHS methods are still more computationally efficient with at least 3.9 times fewer LM iterations than the standard approach. Despite the changes in the quality of the retrievals using the SLM and somewhat the UR-LM method, the LHS technique produced consistent retrievals to that shown in Figs. 7 to 9 and Table 4; and so illustrate the robustness and efficiency of this improved optimization method. Setting the lower bounds to zero should be used with caution as it can underestimate the uncertainty and inflate the average retrieved value, particularly when the value of the model parameter is near zero (*see* Web Appendix B). As such, for operational satellite remote sensing, we advise that the lower bounds of the LM algorithm to be set as slightly negative values.

Discussion

Obtaining a true representation of the uncertainty is crucial for accurate interpretation of ocean color data. The addition of spectral noise to the measured r_{rs} adds more local minima to the solution space that compromises the convergence to the "best" local if not global minimum. We have shown through the inversion of noise-perturbed r_{rs} (sensor-derived and simulated) that the standard approach to LM (SLM) optimization, where the initial guesses are arbitrary and fixed, generated elevated uncertainties because of the convergence to multiple local minima that had different model parameter values. Two methods were presented that searched the multi-parameter space of the BRUCE model, of a given r_{rs}, for the set of parameter values that correspond to a local minimum with the lowest Euclidean distance. The search patterns of these methods differ; in the UR-LM, the optimized values of the inverted r_{rs} were randomly perturbed by 10% of their value and used as the initial guess for a subsequent inversion attempt. This process was repeated until the Euclidean distance fell below 1.0×10^{-5} or if this repetition occurred more than 10 times. In the LHS method, seven sets of initial guesses sampled from the constrained parameter space using Latin Hypercube Sampling were inverted. The optimized values with the lowest Euclidean distance were then used as the initial guesses for the subsequent inversion of noise-perturbed r_{rs}.

Inversions of several HICO derived r_{rs} spectra showed that the UR-LM and LHS method aided the convergence of the LM optimization to one minimum rather than multiple. As a consequence, the estimated uncertainties of the derived IOPs,

depth and bottom albedo decreased and obtained a more accurate representation of the dispersal about the minimum. To test the improvements in accuracy of these two methods (UR-LM and LHS) relative to the SLM approach, we applied these methods to a simulated dataset of r_{rs} spectra whose spectral resolution matched that of HICO. These spectra were generated via forward modeling using the BRUCE model with a range of model parameter values typically encountered in the coastal ocean. Spectrally correlated noise obtained from HICO imagery was added to each simulated r_{rs} to mimic the instrumental noise and imperfect radiometric corrections arising from atmospheric fluctuations and sea surface state. The results showed that the SLM solution approach had substantially lower accuracies, more scatter about true parameter values and higher uncertainties than the UR-LM and LHS methods. Indeed the UR-LM and LHS methods on average increased the accuracies of $a_{phy}(440)$, $a_{dg}(440)$, and $b_{bp}(550)$ by factors of 4, 9, and 14, respectively. On average, the uncertainties for these model parameters were also reduced by factors of 2, 6, and 16, respectively. The retrieved depth also displayed considerable improvement. The SLM method produced accuracies less than 2% for depths greater or equal to 3 m, whereas the LHS method provided accuracies of 51.3%, 11.9%, and 2.3% for depths of 3, 6, and 11 m, respectively. The UR-LM and LHS methods however did not improve retrievals of the bottom albedo coefficients, which have very poor accuracies, high uncertainties, and scatter about the true value. Further analysis revealed that the SLM approach is sensitive to the lower bounds used to constrain the solution space, whereas the LHS (and to a lesser degree, the UR-LM) are considerably more robust and computationally efficient. It should be noted that if spectrally correlated noise is not propagated, and instead just a single reflectance spectrum is to be inverted; then the LHS method would take approximately seven times longer than the SLM. This is due to the search for the optimum initial guess where the LM optimization is performed seven times.

The UR-LM and LHS methods, like the SLM, are susceptible to spectral non-uniqueness as suggested through the set of inversions presented in Fig. 11. In Fig. 11, 2 groups (Groups 1 and 2) of different retrieved depths but similar IO*P* values are present. It is evident that the set of inversions that retrieved a depth greater than 6 m (Grou*p* 2, red data points) had negative B_{sand} and $B_{seagrass}$ values, which are not physically possible. Negative bottom albedo values were retrieved as these model parameters were 'pegged' to the negative lower bounds of the constrained LM optimization. Analysis showed (results not shown here) that when the lower bounds were set to zero, the B_{sand} and $B_{seagrass}$ parameters of Grou*p* 2 only retrieved values of

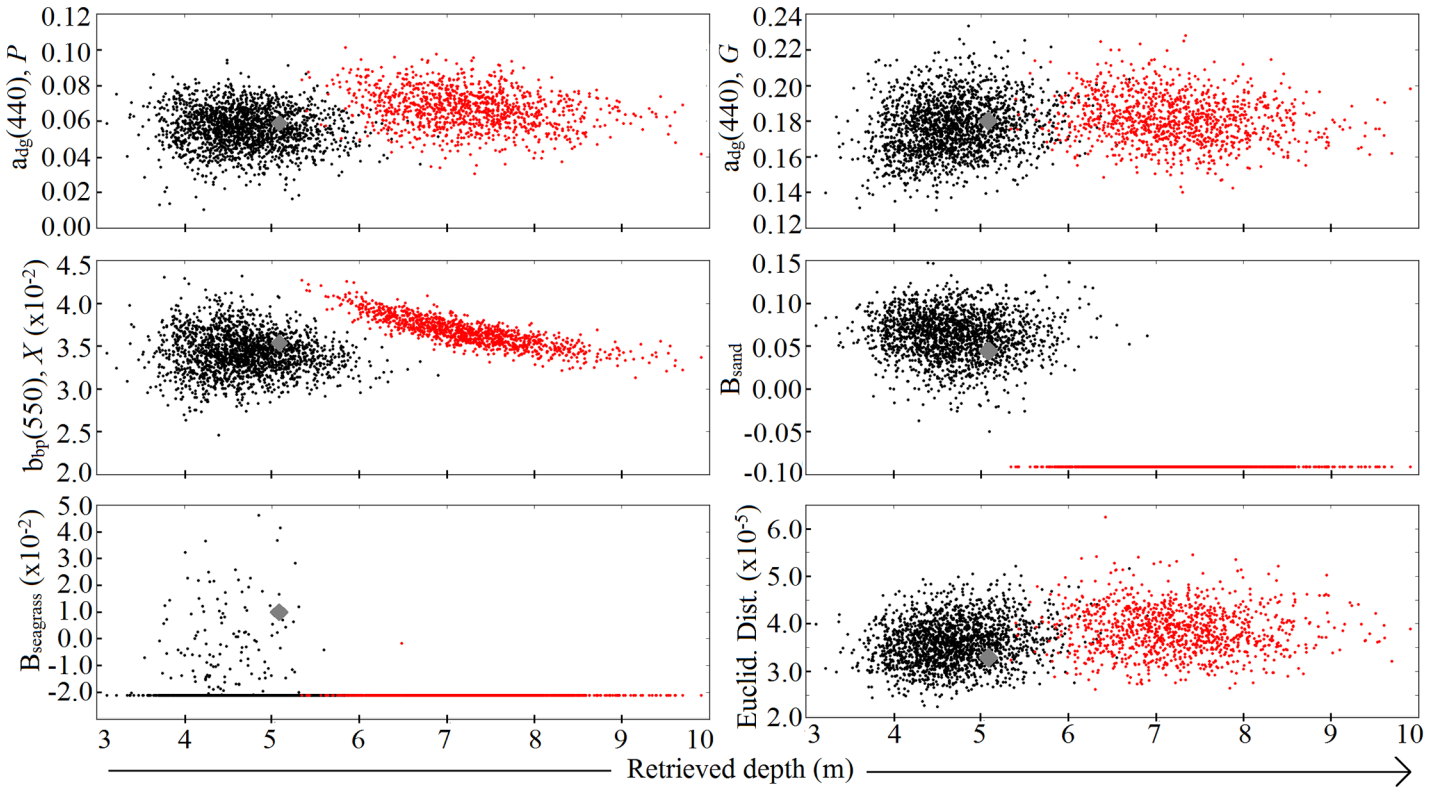

Fig. 11. Non-uniqueness retrieved BRUCE model parameters versus retrieved depth, for the 3000 noise perturbed r_{rs} spectra of quasi-deep HICO pixel at row 1107, column 226, Shark Bay 14-Dec 2011. The optimized guess values were dynamically chosen using the LHS method and are shown as gray diamonds. The red data points (Group 2) have negative B_{sand} and $B_{seagrass}$ that are not physically possible.

zero. The MPFIT algorithm used in this study (Markwardt 2009, Markwardt pers. comm. 2014) pegs a model parameter to an upper or lower bound when the cost function (Euclidean distance) exists beyond that boundary; which for this case implies that the minimum is not physically possible and the retrievals should be ignored or flagged. In the situation shown in Fig. 11, it is possible to determine the correct local minima based on whether the optimization retrieved any model parameters that 'bottomed out.' Situations where two or more minima have very similar Euclidean distances and physically possible model parameters are the limit of optimal remote sensing as Hedley et al. (2012b) describes. For example, from in situ radiometry, it may be possible to identify (through a shallow water model) macroalgae at a shallow depth from sand/seagrass benthos at a deeper depth. However, the satellite/airborne derived r_{rs} spectra of those benthos can contain sensor and environmental noise that can lead not only to indistinguishable spectra but also high uncertainty. These factors can cause the retrieved model parameters of these two benthos to overlap. Although this is an optical remote sensing limit, it is still possible and useful to identify these pixels in the processing using, for example, a post-processing density based cluster analysis, such as DBSCAN (Ester et al. 1996).

Recommendations

Based on the analysis presented, we recommend the use of the Latin Hypercube Sampling (LHS) procedure to search for the optimal initial guess when implementing the LM optimization routine within an optically shallow semi-analytical inversion algorithm. The LHS method is simple to implement, more computationally efficient when using the uncertainty propagation technique, and increases the likelihood of converging to the global minimum relative to the standard approach. Furthermore, the LHS (and to a lesser extent the UR-LM) method converges to a single minimum and affords true representation of the uncertainty caused by sensor and environmental noise. In this article, we used a complex shallow water algorithm that can have up to seven model parameters, and as such it is possible to use the LHS method with other ocean color models (e.g., Generalised IOP model, Werdell et al. 2013) developed for different sensors. Here, we set the number of noise-perturbed spectra to 3000 per pixel when testing the UR-LM and LHS methods on the HICO spectral image data. For operational processing of satellite/airborne imagery, we recommend 50 noise-perturbed spectra per pixel as illustrated in Fig. A10 (Web Appendix A), which in C language takes an average of 0.12 s per pixel using the LHS method on a standard PC without parallel/GPU processing.

References

Albert, A., and C. D. Mobley. 2003. An analytical model for subsurface irradiance and remote sensing reflectance in deep and shallow case-2 waters. Opt. Express. 11(22):2873-2890 [doi:10.1364/OE.11.002873].

Brando, V. E., J. M. Anstee, M. Wettle, A. G. Dekker, S. R. Phinn, and C. Roelfsema. 2009. A physics based retrieval and quality assessment of bathymetry from suboptimal hyperspectral data. Remote Sens. Environ. 49(8):2972-2982.

Ester, M., H-P. Kriegel, J. Sander, and X. Xu. 1996. A density-based algorithm for discovering clusters in large spatial databases with noise. *In* Proceedings of the Second International Conference on Knowledge Discovery and Data Mining (KDD-96). Portland, Oregon, pp. 226–231.

Fearns, P. R. C., W. Klonowski, R. C. Babcock, P. England, and J. Phillips. 2011. Shallow water substrate mapping using hyperspectral remote sensing. Cont. Shelf Res. 31:1249-1259 [doi:10.1016/j.csr.2011.04.005].

Gao, B., M. J. Montes, Z. Ahmad, and C. O. Davis. 2000. Atmospheric correction algorithm for hyperspectral remote sensing of ocean color from space. Appl. Opt. 39(6):887-896 [doi:10.1364/AO.39.000887].

———, and others. 2012. Vicarious calibrations of HICO data acquired from the international space station. Appl. Opt. 51(14):2559-2567 [doi:10.1364/AO.51.002559].

Garcia, R. A., P. R. C. Fearns, and L. I. W. Mckinna. 2014. Challenges in detecting trend and seasonal changes in bathymetry derived from HICO imagery: a case study of Shark Bay, Western Australia. Remote Sens. Environ. 147C:186-205 [doi:10.1016/j.rse.2014.03.010].

Hedley, J. 2008. A three-dimensional radiative transfer model for shallow water environments. Opt. Express. 16(26):21887-21902 [doi:10.1364/OE.16.021887].

———, C. Roelfsema, and S. Phinn. 2010. Propagating uncertainty through a shallow water mapping algorithm based on radiative transfer model inversion. Proceedings of Ocean Optics XX, Anchorage, Alaska.

———, C. Roelfsema, B. Koetz, and S. Phinn. 2012a. Capability of the Sentinel 2 mission for tropical coral reef mapping and coral bleaching detection. Remote Sens. Environ. 120:145-155 [doi:10.1016/j.rse.2011.06.028].

———, C. M. Roelfsema, S. R. Phinn, and P. J. Mumby. 2012b. Environmental and sensor limitations in optical remote sensing of coral reefs: implications for monitoring and sensor design. Remote Sens. 4:271-302 [doi:10.3390/rs4010271].

Helton, J. C., and F. J. Davis. 2003. Latin Hypercube sampling and the propagation of uncertainty in analysis of complex systems. Reliabil. Engng. Sys. Safety 81(1):23-69 [doi:10.1016/S0951-8320(03)00058-9].

Huang, S., Y. Li., S. Shang, and S. Shang. 2013. Impact of computational methods and spectral models on the retrieval of optical properties via spectral optimization. Optics Express. 21(5):6257-6273 [doi:10.1364/OE.21.006257].

Huntington, D. E., and C. S. Lyrintzis. 1998. Improvements to and limitations of Latin hypercube sampling. Prob. Eng. Mech. 13(4):245-253 [doi:10.1016/S0266-8920(97)00013-1].

Kirkpatrick, S., C. D. Gelatt, and M. P. Vecchi. 1983. Optimization by simulated annealing. Science 220(4598):671-680 [doi:10.1126/science.220.4598.671].

Klonowski, W. M., P. R. C. S. Fearns, and M. J. Lynch. 2007. Retrieving key benthic cover types and bathymetry from hyperspectral imagery. J. Appl. Rem. Sens. 1:011505 [doi:10.1117/1.2816113].

Lee, Z. P, K. L. Carder, C. D. Mobley, R. G. Steward, and J. S. Patch. 1998. Hyperspectral remote sensing for shallow waters: 1. A semianalytical model. Appl. Opt. 37(27):6329-6338 [doi:10.1364/AO.37.006329].

———, ———, ———, ———, and ———. 1999. Hyperspectral remote sensing for shallow waters: 2. Deriving bottom depths and water properties by optimization. Appl. Opt. 38(18):3831-3843 [doi:10.1364/AO.38.003831].

Maritorena, S., A. Morel, and B. Gentili. 1994. Diffuse reflectance of oceanic shallow waters: influence of water depth and bottom albedo. Limnol. Oceanogr. 39(7):1689-1703 [doi:10.4319/lo.1994.39.7.1689].

———, D. A. Siegel, and A. R. Peterson. 2002. Optimization of ocean color model for global scale applications. Appl. Opt. 41(15):2705-2714 [doi:10.1364/AO.41.002705].

Marquardt, D. W. 1963. An algorithm for least-squares estimation of nonlinear parameters. J. Soc. Indust. Appl. Math. 11(2):431-441 [doi:10.1137/0111030].

Markwardt, C. B. 2009. Non-linear least squares fitting in IDL with MPFIT, p. 251-254. *In* D. Bohlender, P. Dowler, and D. Durand [eds.], Astronomical data analysis software and systems XVIII, Quebec, Canada, ASP Conference Series, Vol. 411.

Mobley, C. D., and L. K. Sundman. 2000. Hydrolight 4.1 users guide. Sequoia Scientific.

Nelder, J. A., and R. Mead. 1965. A simplex method for function minimization. Computer J. 7:308-313 [doi:10.1093/comjnl/7.4.308].

Press, W. H., S. A. Teukolsky, W. T. Vetterling, and B. P. Flannery. 2007. Numerical recipes: the art of scientific computing, 3rd ed. Cambridge Univ. Press.

Salinas, S. V., C. W. Chang, and S. C. Liew. 2007. Multiparameter retrieval of water optical properties from above-water remote-sensing reflectance using the simulated annealing algorithm. Appl. Opt. 46(16):2727-2742 [doi:10.1364/AO.46.002727].

Slade, W. H., H. W. Ressom, M. T. Musavi, and R. L. Miller. 2004. Inversion of ocean color observations using particle swarm optimization. IEEE Trans. Geosci. Remote Sens. 42(9):1915-1923 [doi:10.1109/TGRS.2004.833389].

Wang, P., E. S. Boss, and C. Roesler. 2005. Uncertainties of inherent optical properties obtained from semianalytical inversions of ocean color. App. Opt. 44(9):4074-4085 [doi:10.1364/AO.44.004074].

Walker, D. I., G. A. Kendrick, and A. J. McComb. 1988. The distribution of seagrass species in Shark Bay, Western Australia, with notes on their ecology. Aquat. Bot. 30:305-317 [doi:10.1016/0304-3770(88)90063-0].

Werdell, P. J., and others. 2013. Generalized ocean color inversion model for retrieving marine inherent optical properties. Appl. Opt. 52(10):2019-2037 [doi:10.1364/AO.52.002019].

Wyss, G. D., and K. H. Jorgensen. 1998. A user's guide to LHS: Sandia's Latin Hypercube Sampling Software. Risk Assessment and Systems Monitoring Department, Sandia Laboratories, Report SAND98-210.

Zhan, H., Z. Lee, P. Shi, C. Chen, and K. L. Carder. 2003. Retrieval of water optical properties for optically deep waters using genetic algorithms. IEEE Trans. Geosci. Remote Sens. 41(5):1123-1128 [doi:10.1109/TGRS.2003.813554].

Submitted 27 February 2014
Revised 24 July 2014
Accepted 27 August 2014